# Exploring the Limits of Boundary Element Methods for Wave Energy Converter Hydrodynamics

Sadie Kass

A thesis

submitted in partial fulfillment of the

requirements for the degree of

Master of Science

University of Washington
2024

Committee:
Curtis J. Rusch
Brian L. Polagye
Michelle H. DiBenedetto

Program Authorized to Offer Degree:
Mechanical Engineering

University of Washington

## Abstract

Exploring the Limits of Boundary Element Methods for Wave Energy Converter Hydrodynamics

Sadie Kass

Chair of the Supervisory Committee:

Curtis J. Rusch
Mechanical Engineering

Boundary element methods (BEM) are used to calculate frequency-domain representations of hydrodynamic forces for moored and floating objects such as wave energy converters (WECs). The representations– excitation, added mass, and radiation damping in up to six degrees of freedom– define and scale the forces in the equation of motion for these devices, and can be used in time-domain modeling tools to predict the behavior of the system in response to waves. It is important for the hydrodynamic estimates to be accurate to determine the viability of a WEC design for energy capture. BEM is a computationally efficient way to calculate these values, using panel methods that only require spatial discretization on the bounding surface. BEM is based on linear potential flow theory, which has assumptions (e.g., linear, incompressible, inviscid, and irrotational flow) that may decrease the accuracy of the hydrodynamic estimates in some conditions. Despite the limitations imposed by these assumptions, results from these BEM codes are widely used in time-domain modeling with little regard for software variability or the suitability of the application. In this thesis, verification and validation procedures were performed on the two most commonly used commercial BEM packages (WAMIT and ANSYS Aqwa) and an open-source package (Capytaine) for four geometries of varying shape. We assess the impact of inter-code variations, mesh variations, and geometric variations on BEM results through grid sensitivity analyses and comparison to experimental results. Solution verification is performed through a mesh sensitivity study using both the grid convergence index and least-squares grid convergence index methods. Solution validation was performed through a comparison to published exper-

imental data for the Sandia WaveBot geometry as a benchmark case. This was followed by comparison to lab-scale experiments for the scaled WaveBot and other hat-shaped geometries. The hat-shaped geometries were defined to keep specific geometric parameters constant to try to determine which parameter is most relevant for comparing results across distinctly different geometries. The eventual goal, beyond the scope of this thesis, is to classify sections of the WEC design space where BEM succeeds and fails.

We show that all three BEM programs produce similar hydrodynamic estimates for all four simulated geometries, indicating that inter-program variability is minor and likely not a large source of uncertainty. The grid convergence study indicates that WAMIT is more sensitive to element size changes than Capytaine, but has <8% change in added mass and radiation damping outputs across all oscillation frequencies and geometries, despite inconsistent convergence at higher frequencies. When compared with hydrodynamic coefficients from the two experimental geometries, BEM performs similarly for each geometry. The results align well at some frequencies, but BEM does fail to capture some behavior when viscous damping or amplitude dependence is present in the experimental data, and disagreements between BEM and experiments increase at higher frequencies. The comparison in BEM parameters across geometries indicates that there could be a connection between the trends in the added mass and radiation damping response with the magnitude of wetted surface area and volume. This thesis is an exploration of what matters in BEM results, and the experimental comparison provides preliminary indications at where BEM might provide sufficient accuracy for WEC modeling.

# Acknowledgements

Thank you to Dr. Curtis Rusch and Professor Brian Polagye for mentorship, support, and advice throughout this project. A special thank you to Sarah Palmer for giving me experimental data and friendship, and being a great running buddy and discussion partner.

I would also like to thank Brittany Lydon for both always providing very positive feedback as I learned these new codes, and providing great insights into the mathematical theory behind the results we are seeing. Thank you also to the other members of the Marine Renewable Energy Lab for your friendliness and good company.

Finally, thank you to Eli, Crow, and my family for providing unconditional support even when you don't know what I am talking about.

Funding for this work was provided by the United States Naval Facilities Engineering Command, in partnership with CalWave.

# DEDICATION

To Crow

# Contents

# List of Figures

# List of Tables

# Chapter 1

# Introduction

## 1.1 Background

With the increasing consequences of global climate change, it is necessary to make the switch to renewable and carbon neutral energy sources as soon as possible. Wind and solar energy technologies are now commonplace with rapidly expanding development, but marine renewable energy sources like ocean waves are still mostly untapped. Among renewables, ocean waves benefit from higher energy density and lower intermittency since they are, essentially, concentrated wind energy transferred into the surface over the ocean over long distances. Because of this, even if the wind is not blowing locally, wind-generated swells from elsewhere propagate with limited energy loss.

Wave energy converters (WECs) are designed to capture this energy, and allow for this energy to be converted into usable forms, like electricity. There is no single standard design for a WEC because there are so many options for energy capture from oscillating systems, but they do fall into some broad categories. A point absorber WEC is a device, generally buoy-type, with an extension that is much smaller than the predominant wavelength of the local wave conditions [1]. Point absorbers can be designed to capture energy due to motion in up to six degrees of freedom (heave, surge, sway, pitch, roll, and yaw) and can consist of a single body or multiple moving in tandem. The float geometries that are the focus of this thesis are most relevant to point absorbers and preliminary experimental comparisons are presented for motion in a single degree of freedom: heave. Heaving point absorbers capture energy by generating a reaction force against

wave-induced motion, either through a connection to the seafloor or a reaction body, such as a heave plate [2]. The portion of the device that converts the heave motion to energy is known as a power take-off (PTO), but the maximum limits of energy capture are set by the geometry and its relationship to the prevailing wave conditions (i.e., distribution of wave heights and periods).

For maximum energy capture in a point absorber, the goal is to ensure that the buoy oscillates within the same range of frequencies as the sea-state and achieves destructive interference with the incident waves. The destructive interference results in energy capture by the WEC PTO, and so to be a good wave absorber, or a good WEC, it must be a good wavemaker [3]. Determining whether a WEC geometry is a good wavemaker relies on estimating the hydrodynamics and motions of buoy in varying wave conditions. Estimations of these dynamics range from low-fidelity simulations, like time-domain modeling in WEC-Sim, to higher-fidelity simulations like computational fluid dynamics (CFD) to tank testing and field deployments. Low-fidelity modeling in WEC-Sim is computationally inexpensive and fast but requires inputs of frequency-domain hydrodynamic coefficients from experiments or simulations. CFD is more of a complete solutions, but has a high computational cost, and does not always increase the fidelity of the estimated hydrodynamic response [4]. Tank testing and field deployments are both expensive and time-consuming, and can introduce unknown uncertainties into results if the methods are not carefully constructed [5]. Therefore, the most often used method for broad investigation of WEC performance and optimization (e.g., [6]) is time-domain modeling.

The most computationally efficient source of frequency-domain hydrodynamics needed for time-domain modeling is boundary element methods (BEM). BEM, when applied to WEC modeling, is a panel method solver that implements potential flow theory, and only requires a mesh on the surface of the buoy. This makes the numerical calculations relatively fast and allows for rapid evaluation of different geometries. The use of linear potential flow theory in BEM means that the fluid and flow is idealized as inviscid, irrotational, incompressible, with linearized boundary conditions. This specifically excludes effects of vortex flows, wave breaking, and of fluid properties like viscous damping. This means that even with non-linear theories and methods accounted for within the time-domain simulation, if the hydrodynamics inputs are linearized, then the output of energy, loading, and motions will not fully capture the nonlinear effects. For this reason, BEM output is often validated with experimental results from laboratory testing or field deployments.

## 1.2 BEM Verification and Validation

Validation of BEM simulations with experimental modeling for WECs has been performed for at least two decades. An early study by Cruz and Salter [7] compared the hydrodynamics of a modified version of the pitching Edinburgh duck geometry to experiments using BEM code WAMIT. They found good agreement in pitch, and good agreement for heave and surge other than near the resonance frequency (i.e., when the damped natural frequency of the pitching WEC matched the frequency of the incident waves). Recent studies for the OES Wave Energy Converter Modelling Verification and Validation task have been conducted for a spherical heaving point absorber with an emphasis on increasing confidence in numerical models of WECs. These are described in Kramer et al. [8], which compares experimental results from highly accurate heave decay tests on a sphere to low-fidelity and high-fidelity simulations for tests that range from linear to non-linear. They find the highest deviation from experiments in the non-linear tests that measure decaying oscillations starting with the sphere out of the water for the potential flow model and suggests that care should be taken when using BEM to describe relatively large amplitude motion.

Studies such as those of Penalba et al. [9] and Raghavan et al. [10] have explored computational variations between commercial and open-source BEM codes for validated geometries to find that most codes have good agreement for a variety of WEC types, especially point absorbers. Penalba et al. includes an exploration of grid convergence as a possible source of disagreement between codes for a two-body point absorber, which falls under the category of solution verification, and is standard practice in most mesh-based simulations. Eskilsson et al. [11] compares solution verification methods for WECs using BEM and higher-fidelity simulations, and proposes a preferred method of estimating the numerical uncertainty due to grid refinement.

Heaving point absorber geometries have been studied in depth, with a focus on optimizing the geometry for the sea-state and to maximize energy capture. Garcia-Teruel and Forehand [12] review hull geometry optimization over the last 20 years, and find frequency-domain BEM methods are most commonly used for point absorber type WECs. This trend continues in recent work. Edwards et al. [6] uses WAMIT with a new theoretical framework to find that optimal geometries are those that protrude outward below the waterline. Shadman et al. [13] performs heaving point absorber geometry optimization to wave conditions for a specific location by using BEM. Jin and Patton [14] compare hydrodynamic response for different

heaving point absorber geometries as a method of optimizing energy capture using BEM coefficients.

Validation of BEM through direct experimental comparison of hydrodynamic coefficients, and estimations of variability between codes, and of grid refinement uncertainty have all been explored for heaving point absorbers. But despite the large body of work that uses BEM for geometry optimization, few to no studies have explored vulnerabilities of BEM with geometry. We aim to validate BEM with experiments for a number of varying geometries under the same wave conditions to try to reveal sensitivities of BEM to geometric features.

## 1.3 Scope of Thesis

To identify areas of inaccuracy in BEM first requires a strong understanding of the theory behind the BEM simulations. This theory is presented in Chapter 2 along with the descriptions of BEM codes, the geometries, and the hydrodynamic parameters of interest. Next, in Chapter 3, an estimation of the uncertainty in the solution due to numerical errors is made through grid refinement analysis, with a deeper exploration into non-standard estimations due to the nature of the BEM problem. This study provides both a baseline error, and a refined mesh that is used in the remaining simulations. With a refined mesh, my operation of the BEM codes is then validated with available BEM and experimental data for a benchmark geometry in Chapter 4. In this chapter, we also present results that show strong similarity in results across BEM codes, demonstrating that they are interchangeable for this application. With a baseline error estimation and validated BEM operation, Chapter 5 presents the lab-scale experimental methods and results. We explore the comparison between the results, and identify possible reasons for agreement and disagreement for different oscillation frequencies, hydrodynamic parameters, and geometries. In Chapter 6 we explore how BEM outputs change with varied geometries. Areas of similarity and differences are tied back to the geometric features of the four geometries and wave conditions. In the discussion, we consider what the relative magnitudes of the results could mean for time domain modeling of WEC designs. Ideas for an overarching parameter that could help define this are discussed. The scope of this thesis is to explore verification and validation of BEM codes, and in doing so begin to identify where the sensitivities and strong points are in the method.

# Chapter 2

# Boundary Element Methods

To understand why BEM is less accurate for some geometries and wave conditions, we must first understand how BEM works and what assumptions are involved in the theory. Each BEM code has slightly different options and implementation, and these differences are presented. We then identify the hydrodynamic parameters used in this study, which relate strongly to geometry. Finally, we define the chosen float geometries and the reasoning behind the choice.

## 2.1 BEM Theory

There are a number of commercial and open-source BEM codes for hydrodynamics in use today. Three of these codes are ANSYS Aqwa, WAMIT, and Capytaine. Each code has a slightly different array of options that enable higher accuracy or more "realistic" simulations, but the mathematical theory behind the bulk of the operations is the same. The following mathematical description is primarily a rephrasing and summary of the mathematical theory of BEM as presented in the Aqwa [15] and WAMIT [16] theory manuals, following the program specific notation of WAMIT. There are small differences in how the BEM theory is presented and implemented between these programs, but the overall theory holds true regardless of these variations.

The underlying theory of BEM for hydrodynamics is linear potential flow. The assumptions of potential flow are that the fluid is incompressible, and the flow is irrotational, thus the flow is inviscid. In this formulation, inviscid means there are no viscous forces, incompressible assumes no density changes, and irrotational flow means the flow has no vorticity. These assumptions allow for the creation of a velocity

potential function ($\nabla\Phi$), which with the continuity equation satisfies the Laplace Equation:

$$\nabla^2\Phi = 0. \tag{2.1}$$

With the additional assumption of body and fluid motions with harmonic time dependence, this velocity potential can be written as the real component of a complex velocity potential ($\varphi$):

$$\Phi = Re(\varphi e^{i\omega t}) \tag{2.2}$$

where $\omega$ is the angular frequency in radians per second, $t$ is time, and $i$ is the imaginary number $\sqrt{-1}$.

We additionally assume that motions are small amplitude, and thus the free-surface and body boundary conditions can be linearized. For the same reason, linear superposition holds and the complex velocity potential can be broken down into potentials associated with different physics. The radiation potential ($\varphi_R$), represents the oscillatory motions of the body in all three translational (surge, sway, heave) and rotational (roll, pitch, yaw) degrees of freedom, with no incident waves, and thus is separated by these degrees of freedom. The diffraction potential ($\varphi_D$), represents the motions of the free-surface on a fixed body due to incident waves and can be broken down into the addition of incident wave potential ($\varphi_0$) from Airy wave theory, and scattering potential ($\varphi_S$), which is the disturbance of incident waves by the fixed body at its undisturbed position. In aggregate,

$$\varphi = \varphi_R + \varphi_D = \varphi_R + \varphi_0 + \varphi_S. \tag{2.3}$$

For the purposes of experimental comparison, only the total diffraction potential ($\varphi_D$) will be considered, as the decomposition into scattering and incident wave components is not possible with experiments.

This boundary value problem is subject to the additional boundary conditions of the seabed surface condition ($\frac{\partial\varphi}{\partial z}$ = 0 at z=0), the free-surface condition (body has little or no forward speed), and the radiation condition where wave disturbance dissipates with distance. To get a continuous boundary integral equation to solve for these velocity potentials that satisfies the boundary conditions, Green's Theorem is used, where the Green's function ($\mathbf{G}(\xi; x)$) is the velocity potential at point $x$ due to a point source of strength $4\pi$ located

at point $\xi$. This source distribution method creates the following boundary integral equations for radiation and diffraction potentials:

$$\varphi_R = \frac{1}{2\pi}\int_{S_B}\varphi(\xi)\frac{\partial \mathbf{G}(x;\xi)}{\partial n_\xi}dS_B - \int_{S_B}\mathbf{G}(x;\xi)\frac{\partial\varphi(\xi)}{\partial n_\xi}dS_B \tag{2.4}$$

$$\varphi_D = \frac{1}{2}\varphi_0(x) - \frac{1}{2\pi}\int_{S_B}\varphi(\xi)\frac{\partial \mathbf{G}(x;\xi)}{\partial n_\xi}dS_B \tag{2.5}$$

where $S_B$ is the wetted surface at its mean position. The variable $n$ refers to the unit normal vector from the body's surface. In rotational degrees of freedom, $n = r \times n$, where $r$ is the position vector of a point on the hull relative to the body center of gravity [15]. If the velocity potential is then approximated by a distribution of sources over the mean wetted surface only, these equations simplify to the following:

$$\varphi(x) = c\int_{S_b}\sigma(\xi)\mathbf{G}(x;\xi)dS_B \tag{2.6}$$

where $\sigma$ is the source strength, and $c$ is a factor of 1, $\frac{1}{2\pi}$, or $\frac{1}{4\pi}$ depending on the location of the panel in relation to the still water line, and program specific conventions.

To numerically solve these equations, the mean wetted surface is discretized into a mesh of quadrilateral or triangular elements. These elements are not inherently planar, but if sufficiently refined, curvature is minimal [16]. The midpoints of the elements are used to project the elements into planar panels that are used for the calculation. The source strength, radiation potential, and velocity potentials are taken to be constant over these panels. The discrete form of Eq. 2.6 is:

$$\varphi(x) = \sum_{m=1}^{N_p}\sigma_m\mathbf{G}(x;\xi_m)\Delta S_m \tag{2.7}$$

where $N_p$ is the number of panels.

## 2.2 BEM Codes

The three BEM codes validated in this study are ANSYS Aqwa, WAMIT, and Capytaine. ANSYS Aqwa and WAMIT are commercial codes and were chosen for this study because they represent the industry standard

for BEM on WECs. Capytaine is an open-source code adapted by Ancellin and Dias [17] from BEM code Nemoh [18] and was chosen partially as a contrast to the well-established commercial codes, and due to simplicity in installation and operation. Eq. 2.7 is implemented in all three BEM codes, but with small variations and additional tools used to simplify the computation. For example, in the case of ANSYS Aqwa and Capytaine, the complex velocity potential is the complex conjugate of the one from WAMIT that is described in the previous section. Similarly, WAMIT requires a meshed geometry file to be prepared with inward facing normal vectors on the panels [16] while Aqwa and Capytaine expect normal vectors facing outwards from the buoy hull.

ANSYS Aqwa was originally a separate program written for seakeeping analysis and motions by WS Atkins in 1971, but has since been acquired by ANSYS and integrated into ANSYS Mechanical and Workbench [19]. Aqwa includes separate analysis systems for frequency and time-domain modeling. The time-domain analysis system is 'Hydrodynamic Response'. The BEM portion of the code refers to the frequency-domain analysis system, 'Hydrodynamic Diffraction'. This code can be accessed from the command line or using the GUI with Workbench. With the limited time-span of this project, Aqwa was solely accessed with the GUI, to allow for quick methods checks and visualization. As Aqwa is an integrated ANSYS product, there are standard geometry definition, modeling, and mesh creation tools that automatically transfer information to the Hydrodynamic Diffraction module. Aqwa also allows external geometry files to be imported, but not meshes. Aqwa allows the removal of spurious responses at certain frequencies ("irregular frequencies") that arise due to the numerical methods through the generation of an internal lid at the waterline. BEM simulations in Aqwa require the specification of wave directions and frequencies, and you can set the depth of your fluid domain. Along with the other two codes, Aqwa requires the geometry to be defined at its natural buoyant position at the still water line with the z-axis pointing upwards.

WAMIT is a BEM program created by MIT in 1987, with six updated versions with greater capabilities released since [16]. WAMIT is accessed through the command line with prepared input files. Simulation results, similarly, are returned with output files. While computation occurs, the command window displays text with warnings or updates as the code runs, which is the only graphical output offered. The WAMIT simulations are separated into a potential solver and a force solver. The potential solver requires many more calculations, and transfers the data to the force solver when completed. Preparation tools for creating

a meshed geometry file in GDF format are available as add-ons with licensing, but alternative external programs can be used for the same preparation, such as Rhinoceros (Rhino). Rhino was used in tandem with an ANSYS modeling product to produce the GDF files for this study. In addition to the source distribution BEM method outlined above, known as the low-order method in WAMIT, the code includes a high-order method that represents the velocity potential on the panels as continuous B-splines instead of a constant value [16]. However, to directly compare BEM codes, only the low-order method is used in this study. WAMIT allows for the removal of irregular frequencies with multiple methods, the easiest is by allowing it to define the waterline nodes automatically. Like Aqwa, WAMIT requires a definition of wave directions and frequencies, but it is important to note that it expects an input of wave period.

Capytaine is a BEM code implemented in Python in 2019, with the most recent version released in 2024 [17]. As with other Python codes, Capytaine can be accessed in a virtual environment or directly through scripts created on the local device. All packages and dependencies are either included in the installation, or easily installed from the internet. Visualization is possible with standard Python plotting packages, and the data output format is the standardized NetCDF data structure. Capytaine allows geometry and mesh import in a number of formats, but does not contain a creation tool within the core package. Unlike WAMIT and Aqwa, Capytaine requires a manual definition of which degrees of freedom the user wishes to be computed, which can decrease the computation time and volume of data. Capytaine does not yet have a method of removing irregular frequencies but [20] presents a number of methods to correct for this in post-processing. For this study, I primarily interfaced with Capytaine through the integration with WecOptTool by Sandia National Labs [21], though I did explore some of the settings that were not available through that layer.

Many of the required inputs for these simulations are the same across programs. The frequency range that we defined for this study is from approximately 0.66 Hz - 2.65 Hz, which is a Froude-scaling of the frequency range of the benchmark experimental data. All three BEM codes require us to specify the location of the center of mass in the geometry. Though it does not necessarily mirror the experimental models, this center of mass is determined from the geometry. The center of rotation is set to the same location where possible. We remove irregular frequencies in both Aqwa and WAMIT simulations. A more detailed list of settings is available in Appendix A.

## 2.3 Hydrodynamic Parameters

The time domain equation of motion for a WEC describes all of the forces on the given body. These are due to gravity, buoyancy, excitation from incident and diffracting waves, drag, machinery forces, mooring forces, and more [1]. For this study we are concerned with the impact of the geometry of the body on the motions, so we neglect machinery forces, mooring forces, and non-wave environmental forces, resulting in :

$$M_{ij}\ddot{x}_i + K_{ij}x_i = F_i \tag{2.8}$$

where $x_i$ is position in $i$ degrees of freedom, the dot notation refers to the first and second time derivatives, $M_{ij}$ is the inertia matrix from the mass distribution, and $K_{ij}$ is the hydrostatic stiffness matrix associated with buoyancy. The $ij$ notation here refers to a change force in direction $i$ due to motion in direction $j$. $F_i$ refers to the external forces: Froude-Krylov forces from incident waves, diffraction, and radiation forces for each degree of freedom $i$. These external forces can be found in the frequency domain with BEM, and are key in estimating the potential power absorption of a WEC design. This equation of motion converted to the BEM frequency-domain form by the Fourier transform is given as:

$$[-\omega^2 M_{ij} + K_{ij}]X_j = F_i \tag{2.9}$$

where $X_j$ is the amplitude in the relationship $x(t) = Re[X_j e^{i\omega t}]$ [17]. The external forces can be broken into the addition of Froude-Krylov ($F_{FK}$), diffraction ($F_D$), and radiation forces ($F_R$). The Froude-Krylov and diffraction forces can be combined to a single wave excitation force because they are both the forces on a still body due to incoming waves (both incident and diffracting). This combined wave excitation force is one of the key hydrodynamic parameters used for comparison in this study and exists in six degrees of freedom.

The radiation forces are the forces felt by the body when moved in still water [1]. The radiation force can be further decomposed into an added mass matrix ($A_{ij}$) proportional to acceleration, and a radiation damping matrix ($B_{ij}$) proportional to velocity, resulting in the following equation for radiation force:

$$F_R = [\omega^2 A_{ij} + i\omega B_{ij}]X_{ij}. \tag{2.10}$$

Added mass and radiation damping are the other two key hydrodynamic parameters of interest for this study. Added mass can be thought of as the amount of mass entrained with the body motion. This can change the natural frequency of the WEC, thus changing the range of frequencies for optimal energy capture, which makes this parameter essential in WEC design. Radiation damping is related to the amplitude of waves radiated from the body when it moves. This amplitude is strongly tied to power capture, as the interference of the radiated waves with the incident waves allows for energy capture, and therefore must be accurate for effective WEC modeling. Added mass and radiation damping are both induced by rigid body motions in one degree of freedom, which results in entrained mass or motion in a reactive degree of freedom, so there are 36 values for each coupling of these degrees of freedom in each 6x6 coefficient matrix. Some degrees of freedom are more strongly coupled than others, but for this study we are only looking at matching induced and reactive degrees of freedom (e.g., heave-heave).

The excitation forces, radiation damping coefficient matrix, and added mass matrix are found in BEM by using the radiation and diffraction potentials. When wave potentials are known, so is the first-order hydrodynamic pressure distribution ($p^{(1)}$) from the linearized Bernoulli equation:

$$p^{(1)} = -\rho \frac{\partial \Phi}{\partial t} = i\omega\rho\varphi(x)e^{i\omega t} \tag{2.11}$$

where $\rho$ is water density.

By integrating the pressure distribution over the wetted surface, the fluid forces corresponding to the velocity potentials can be determined. These fluid forces describe the loads and motions of the object and affect the energy that can be extracted from the motion of the WEC. From the diffraction potential, the Froude-Krylov forces and moments due to the incident wave can be determined for each seakeeping degree of freedom, and separately the scattering or diffraction forces due to the diffraction wave can be found in each degree of freedom. These are governed by the following equations:

$$F_{FK,i} = -i\omega\rho \int_{S_B} \varphi_0(x) n_i \, dS_B \tag{2.12}$$

$$F_{D,i} = -i\omega\rho \int_{S_B} \varphi_S(x) n_i \, dS_B \tag{2.13}$$

which are also estimated by the discretization of the mean wetted surface (Eq. 2.7).

From the radiation potential, the radiation force or moments of the radiation wave induced by a rigid body motion in j degree of freedom can be determined for each degree of freedom. This is governed by:

$$F_{R,i,j} = -i\omega\rho \int_{S_B} \varphi_{R,j}(x) n_i \, dS_B \tag{2.14}$$

where this equation is repeated for each combination of i, j, degrees of freedom for a total of 36 radiation force values. The radiation potential can be further decomposed into real and imaginary components. This allows for the separation of the added mass (imaginary) and radiation damping (real) coefficients when integrated over the body surface as is shown in Eq. 2.10.

The wave excitation force, added mass, and radiation damping coefficients are calculated as a function of frequency in BEM, which allows for a complete picture of WEC motions in an irregular wave spectrum. Following the calculation of these three coefficients, we have a solution for all the unknowns in the equation of motion from hydrodynamic force. When combined with design parameters, such as PTO mechanical damping and stiffness, we can solve the time-domain equation of motion to simulate WEC performance.

## 2.4 Description of Geometries

In this study, we use BEM simulations of multiple buoy geometries to understand the impact of geometry on the accuracy of hydrodynamic parameters calculated using BEM. We are specifically interested in better understanding the geometric features that may invalidate BEM assumptions, thus resulting in inaccurate results. To determine the geometries for testing, we conducted a thorough review of existing experimental-BEM comparison papers to identify geometries that were uncommon, or of interest. An initial evaluation of geometries through BEM was performed to further narrow the design space by finding geometries that exhibit differing hydrodynamic behaviors. At the time of this thesis, two geometries have been experimentally tested, and four geometries simulated with BEM.

Before thoroughly sampling the design space to determine these geometries, we sought to run a baseline check of our BEM codes against a geometry with published results. For this, the Sandia National Labs "WaveBot" was chosen, as it has available experimental data for comparison, reports containing plots with BEM validation, and is a geometry that is relatively easy to model while still being feasible for a commercial

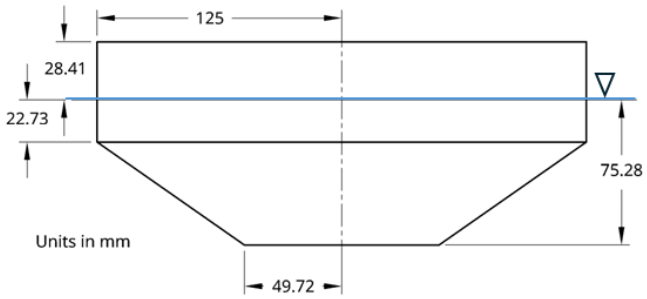


**Figure 2.1:** Lab-scale WaveBot geometric definition

WEC design. WaveBot was designed by Sandia for some of the aforementioned reasons, as a test case for generating control schemes for lab experiments, and evaluating hydrodynamics of heaving point absorbers through multiple degree of freedom experimental testing [22]. A quick overview of the Sandia experimental testing used for comparison is given in Chapter 4, and more information can be found in the 2016 test report [23]. The WaveBot is not a functional WEC; it has no PTO and the model used in the 2016 report is made of wood at approximately 1/17 scale of a hypothetical commercial WEC [23]. Due to the constraints of the UW experimental facilities, the WaveBot in the following simulations is a further 1/7 scale of Sandia's device (i.e., a 1/119 scale of the commercial concept), with dimensions as shown in Figure 2.1. While relatively small scale, experimental testing has been carried out to gain insight at up to 1/100 scale [24].

The second geometry was determined by the literature review, and is a variation on the common cylindrical buoy design as seen in Figure 2.2. The shape is a cylindrical buoy with a submerged lip, as we anticipated that this lip could induce viscous and nonlinear behavior in water. This shape is a tall cylinder of smaller diameter with a wider and shorter cylinder of equal diameter to the waterline diameter of WaveBot at the bottom, resembling a top hat. The entire composition is of equal draft to WaveBot, measured from the still waterline. This geometry will be referred to as the 'Hat' for the remainder of this thesis. The geometric dimensions of the equal draft and diameter hat are shown in Figure 2.2.

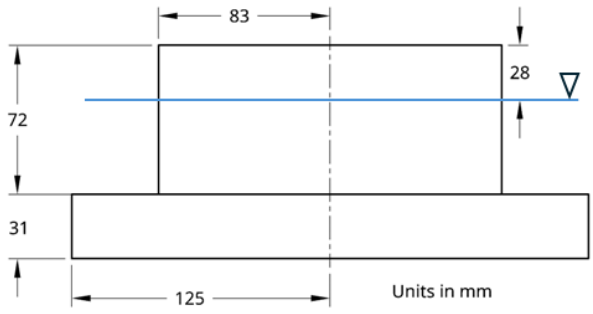


**Figure 2.2:** Geometric definition of the hat buoy with equivalent characteristic diameter and draft to WaveBot

The third and fourth geometries were chosen to be a variation on the hat to investigate which geometric scaling parameters matter most in BEM results. Scaling parameters in this case are the geometric parameters such as submerged volume, surface area, or diameter that can be held constant when varying geometries. Determining the most relevant parameter here can help us make a more direct comparison between results for different geometries.

The third geometry is a hat shape with submerged volume held constant with WaveBot with dimensions shown in Figure 2.3. The largest diameter of the hat is also held constant.

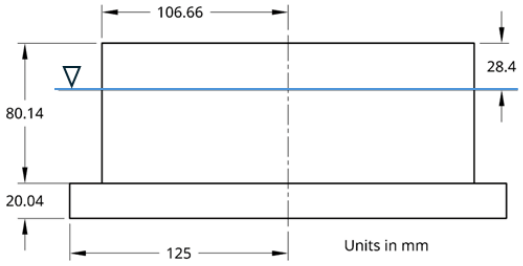


**Figure 2.3:** Geometric definition of the hat buoy with equivalent submerged volume to WaveBot

The fourth geometry is also a variation on the hat, with the wetted surface area held constant with WaveBot with dimensions shown in Figure 2.4. We chose this parameter to hold constant because the integral of velocity potential in BEM theory is over the wetted surface area. There are an infinite number of possible geometries that could be generated in the hat shape with this area, but this geometry keeps the

same characteristic diameter of the lip of the hat to WaveBot resulting in a flat hat-shaped disc.

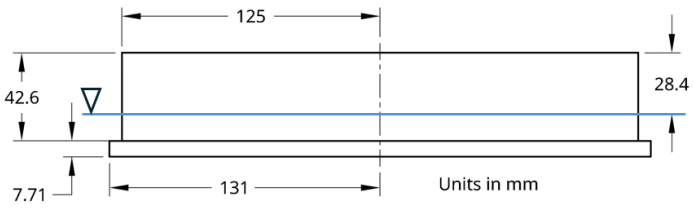


**Figure 2.4:** Geometric definition of the hat buoy with equivalent wetted surface area to WaveBot

The ANSYS DesignModeler tool was used to model these geometries for use in BEM. As we discuss later in this thesis, the same mesh is used for each BEM code, so only one modeling and meshing tool is necessary for geometry generation.

# Chapter 3

# Grid Refinement Analysis

To ensure that simulation results are accurate and precise, solution verification and validation studies are performed to estimate the uncertainty in the numerical calculations. Solution *validation* is ensuring the accuracy of a numerical model in representing the real-world application. Solution *verification* is ensuring precision by estimating the uncertainty in a simulation due to numerical discretization and approximations of continuous functions. Solution validation is performed in Chapter 4 through comparison to benchmark experimental results. Solution verification is usually performed through a grid refinement study involving the spatial mesh and/or temporal resolutions. For this application, the spatial mesh is the relevant source of error, as seen in the discretization of the surface integral in Eq. 2.7, where the wetted surface is approximated by a number of panels.

The discretization of Eq. 2.7 requires a mesh of triangular or quadrilateral elements that are both of good quality and sufficiently refined. To determine the mesh quality, many computational tools that use meshes have built in quality checks that ensure that individual elements and the ratios of element shapes meet minimum requirements, such as skewness (i.e., distortion of the shape from a equilateral element) and aspect ratios. The mesh must be sufficiently refined so that the projected planar panels from the mesh elements are indicative of the true shape of the object (e.g., in an extreme case, attempting to represent a sphere with six elements, would render it as a cube) [16]. The common procedure to ensure that a mesh is sufficiently refined is to perform a grid refinement study using the classical grid convergence index (GCI) by Roache [25]. This results in both an estimation of uncertainty due to numerical discretization for a

fine and coarser mesh, and helps to inform which mesh is refined enough for your application. A more flexible variation of the GCI method that allows for second-order and mixed convergence was developed in recent years by Eça and Hoekstra [26] using least-squares methods. This LS-GCI method has recently been shown to be more effective for WEC applications by Eskilsson et al. [11] due to its flexibility with different convergence rates. For this reason, the GCI method, LS-GCI method, and a more qualitative estimation of convergence were all performed for each geometry for each BEM code to give a comprehensive view of solution verification for BEM.

## 3.1 Mesh Generation

To properly evaluate the sensitivity of the mesh to refinement for each program, the same mesh was imported into each of the BEM codes. This eliminates variation that is due to different element shapes and aspect ratios, so the results should only reflect code-specific grid resolution sensitivity. For the three BEM codes studied, Aqwa had the least flexible mesh import options, so the meshes were created in the standard ANSYS meshing module and converted into readable formats for Capytaine and WAMIT (.stl and .gdf formats, respectively). The ANSYS mesh creation tool for hydrodynamics meshes allows the user to control mesh element size and shape of mesh elements. For every mesh in this study, triangular elements are used since these can more easily approximate irregular shapes, and can be exported as an .stl file without changes to the mesh. The refinement sizes chosen have a constant ratio of consecutive element sizes $h_i$ and $h_j$, or refinement ratio of $r = h_i/h_j = \sqrt{2}$, and the coarsest mesh size was chosen to just approximate the smallest length scale in all of the geometries (the height of the lip of the equal surface area hat). The mesh sizes, number of elements, and number of submerged or diffracting elements is shown below in Table 3.1. Aqwa imposes a maximum number of submerged or diffracting elements at 30,000, but given the relative simplicity of our geometries, the mesh refinement study proves that further refinement beyond around 10,000 elements was not necessary.

To import into Capytaine, the mesh was simply exported from Aqwa in an .stl format. To import into WAMIT, the .stl file needed to be read into a program that could convert it into a .gdf file. We used Rhino, a modeling and meshing program used for both engineering and artistic applications. To prepare it for WAMIT, the meshes were sliced at the waterline so that only the submerged cells remained. The separation

**Table 3.1:** Statistics of meshes used in grid convergence study

| Shape | Element Size [m] | $\underline{h}_j$ | Number of Elements | Number of Sub. Elements |
|---|---|---|---|---|
|  WaveBot | 0.01414 | 2.828 | 1684 | 922 |
| | 0.01 | 2 | 3468 | 1945 |
| | 0.00707 | 1.414 | 6922 | 3718 |
| | 0.005 | 1 | 13974 | 7576 |
|  Equal Draft Hat | 0.01414 | 2.828 | 1844 | 1453 |
| | 0.01 | 2 | 3560 | 2804 |
| | 0.00707 | 1.414 | 7068 | 5360 |
| | 0.005 | 1 | 13872 | 10537 |
|  Equal Volume Hat | 0.01414 | 2.828 | 1936 | 1261 |
| | 0.01 | 2 | 3806 | 2355 |
| | 0.00707 | 1.414 | 7352 | 4681 |
| | 0.005 | 1 | 15010 | 9596 |
|  Equal Surface Area Hat | 0.01414 | 2.828 | 1698 | 958 |
| | 0.01 | 2 | 3334 | 1837 |
| | 0.00707 | 1.414 | 6914 | 3733 |
| | 0.005 | 1 | 13666 | 7369 |

of the geometry at the waterline in ANSYS during modeling ensured that there were no open or low quality elements after this slicing operation. To verify this, the Rhino 'mesh check' tool was used on each mesh. The number of elements in the mesh now is equal to the number of submerged elements in Aqwa. Next, the direction of the unit normal vectors of the cells had to be flipped, as WAMIT requires them to be inward facing for its calculations. The unit normals likely need to be flipped if WAMIT produces the error:

```
Warning:  body volume less than 1.E-30 for body N=1.
```

With the meshes imported into each program, the GCI and LS-GCI methods described in the next section are completed the same way in each BEM code. Representative meshes for each of the four geometries is shown in Figure 3.1

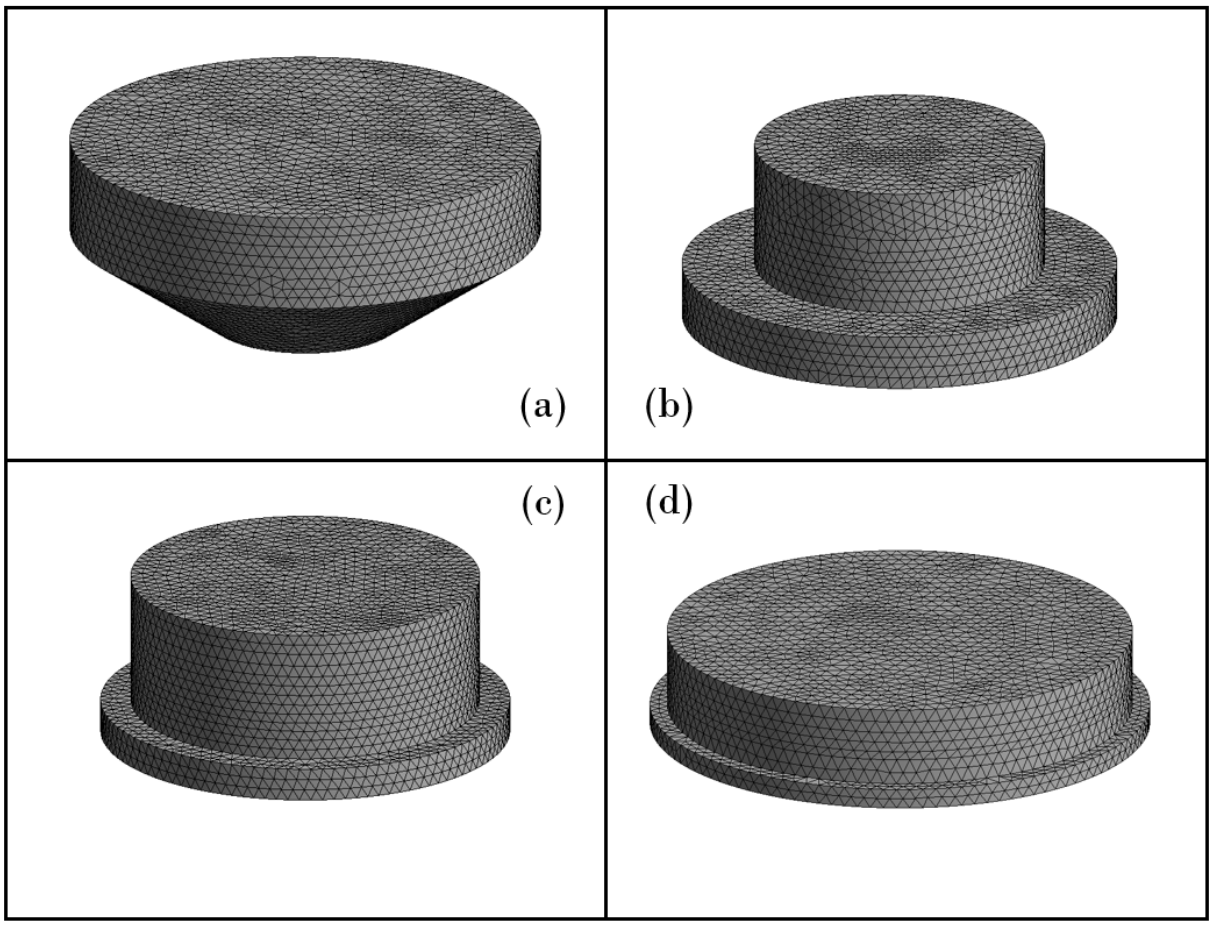


**Figure 3.1:** Representative meshes for each geometry: (a) WaveBot, (b) Equal Draft Hat, (c) Equal Volume Hat, and (d) Equal Surface Area Hat. Note: These are the optimal meshes identified by the refinement study and are used for simulation validation.

## 3.2 GCI Method

The GCI method for estimating numerical error and corresponding uncertainty ranges in grid convergence studies was established by Roache in 1997 for CFD and other numerical simulation applications [25]. This method calculates the numerical error ($\delta$), which is defined as the difference in a numerical result ($\psi_i$) and exact result ($\psi_0$) for a given parameter ($\psi$). The numerical error is scaled by a safety factor to become numerical uncertainty, ($U_\psi$). Numerical uncertainty defines the interval that should contain the exact solution as:

$$\psi_i - U_{\psi_i} \leq \psi_0 \leq \psi_i + U_{\psi_i} \tag{3.1}$$

The following theory is summarized from Roache [25]. The GCI method requires a constant refinement ratio ($r$) across all meshes. This ratio is defined by the ratio of representative element sizes of two meshes. This is equivalent to the ratio of cell sizes ($\underline{h_i}$) that have been non-dimensionalized by the finest element size ($\underline{h_i} = h_i/h_1$).

$$r = \underline{h_i}/\underline{h_j} \tag{3.2}$$

For our application, $h$ is the element size defined in the ANSYS meshing tool.

Common values for the refinement ratio are 2 and $\sqrt{2}$, the latter being adopted to keep the number of elements from increasing too quickly. Practically, any value greater than 1 should suffice, though this could require a relatively large number of meshes to establish convergence. The next step is to estimate the convergence rate or order of accuracy of the method ($p$). To get a fully defined estimation for $p$ requires results from three meshes:

$$p = \frac{ln(\frac{\Delta_{2-3}}{\Delta_{2-1}})}{ln(r)} \tag{3.3}$$

where $\Delta_{i-j} = \psi_i - \psi_j$. This convergence rate should be asymptotic for the GCI method to succeed, which is defined as between 0.95 and 2.05. The convergence is further required to be monotonic, not oscillatory, and so convergence cannot fluctuate. If these conditions are met, we can use Richardson extrapolation to estimate the converged value $\psi_0$ as:

$$\psi_0 = \psi_1 + \frac{\psi_1 - \psi_2}{r^p - 1} \tag{3.4}$$

and estimate the numerical error for the most refined mesh ($\delta^1$) as:

$$\delta^1 = \psi_1 - \psi_0 = \frac{\Delta_{2-1}}{r^p - 1} \tag{3.5}$$

where the 0 in $\psi_0$ represents the theoretical converged mesh state.

These numerical errors are converted to uncertainties through the multiplication of a safety factor. Roache determines a safety factor of 1.25 is sufficient for calculations with three or more meshes, such that:

$$U_\psi^1 = 1.25|\delta^1| = \frac{1.25|\Delta_{2-1}|}{r^p - 1} \tag{3.6}$$

and

$$U_{\psi}^{2} = 1.25|\delta^{2}| = \frac{1.25|\Delta_{2-1}|r^{p}}{r^{p}-1} \tag{3.7}$$

If we define an acceptable level of error in the simulation, we can choose the least refined mesh that falls within that range of uncertainty.

## 3.3 LS-GCI Method

The LS-GCI method has been continually improved since the original work by Eça and Hoekstra [26], with the most recent update in 2019 [27] [28]. The method relies on approximating the error with a least-squares fit instead of a simple difference as:

$$\delta_{RE} = \psi_i - \psi_0 = a\underline{h}_i^p \tag{3.8}$$

where $p$ is the order of convergence and $a$ is a coefficient determined by the least squares fit. A first order convergence would have $p = 1$, second order $p = 2$, and a mix of first and second order would result in a weighted summation of terms with $p = 1, 2$. The exact equations for calculating the coefficients ($a$), converged values ($\psi_0$), and errors ($\delta_{RE}$) are described in detail in [27]. These are non-trivial equations to solve, but there is a freely accessible code created by Eça and Hoekstra and the Maritime Research Institute Netherlands (MARIN) called "Numerical Uncertainty Analysis" that automates this analysis based on an input of chosen parameter values at each mesh resolution [29].

The key aspect of the LS-GCI method is its ability to solve for uncertainty with monotonic, oscillatory, and anomalous convergence behavior. For the monotonic behaviour, they additionally are able to estimate error when $p < 0.95$ or $p > 2.05$. Consequently, the error estimates for first and second order convergence are appropriate for monotonic convergence outside the GCI range [27], and the mixed convergence for oscillatory behavior. The error estimates are converted to uncertainty ranges based on the “quality” of the error estimation using a more complicated approach than the simple safety factor proposed by Roache. The details of this are left to the interested reader to explore [27].

## 3.4 Results

To evaluate the impact of mesh refinement on the BEM results, the relevant parameters for determining mesh convergence were chosen to be the same hydrodynamic parameters used in BEM validation (Chapter 5): added mass and radiation damping in heave. These parameters were sampled at five frequencies across the frequency range, and grid convergence was tested at each sampled frequency.

Results using the GCI method for the mesh of element size $0.00707$ m (second most refined mesh) are provided in Table 3.2. Aqwa results are not included because the mesh quality checks within the program are too strict for the capabilities of the ANSYS Meshing tool, and not all meshes could be used in the simulations, specifically those that are more refined. The uncertainty results from the equal surface area hat are not included here because this version of the equal surface area hat is not the version that will be used for future experimental testing.

**Table 3.2:** Estimated discretization uncertainty of added mass ($U_{AM}$) and radiation damping ($U_{RD}$) for three geometries in heave by the GCI method in Capytaine (CP) and WAMIT (WM). Dashes indicate convergence cases that did not meet the requirements of the GCI method.

| **Shape** | **Code** | **Uncertainty** | **0.66 [Hz]** | **1.147 [Hz]** | **1.635 [Hz]** | **2.163 [Hz]** | **2.65 [Hz]** |
|---|---|---|---|---|---|---|---|
|  WaveBot | CP | U_AM [%] | 0.40 | 0.41 | 0.56 | 0.24 | 2.09 |
| | WM | U_AM [%] | 0.12 | - | - | - | - |
| | CP | U_RD [%] | - | - | 1.08 | 4.56 | 3.81 |
| | WM | U_RD [%] | 0.28 | - | - | - | - |
|  Equal Draft Hat | CP | U_AM [%] | - | - | - | - | - |
| | WM | U_AM [%] | 0.87 | 1.09 | 0.79 | 0.58 | - |
| | CP | U_RD [%] | - | - | - | - | - |
| | WM | U_RD [%] | 2.65 | 13.58 | 3.52 | 1.81 | 1.58 |
|  Equal Volume Hat | CP | U_AM [%] | - | - | - | - | - |
| | WM | U_AM [%] | 0.91 | 1.21 | 1.50 | 1.38 | 1.25 |
| | CP | U_RD [%] | - | - | - | - | - |
| | WM | U_RD [%] | 0.69 | 2.57 | 14.12 | 19.73 | 8.98 |

As stated previously, for the GCI method to produce an uncertainty estimation, the convergence rate must be in the range of 0.95 to 2.05, and be both asymptotic and monotonic. For each case, despite sampling at five frequencies per parameter, the convergence rate was rarely in that range for either radiation damping or added mass for all geometries. Specifically, for the WaveBot geometry, there was monotonic convergence at all five frequencies for added mass calculated with Capytaine. For the equal volume and equal draft hats,

monotonic convergence occurred for WAMIT at most frequencies. All other code and parameter pairings for the three geometries resulted in non-monotonic convergence at all but a few of frequencies, with the absence of an uncertainty estimate indicated with dashes in Table 3.2. This is consistent with prior results reported by Eskilsson et al. [11] who found that the WEC hydrodynamics problem often produces oscillatory convergence, and is not well suited for the GCI method.

Table 3.3 shows the results for the mesh of element size $0.00707$ m by the LS-GCI method for the first three geometries in heave for two BEM codes.

**Table 3.3:** Estimated discretization uncertainty of added mass ($U_{AM}$) and radiation damping ($U_{RD}$) for three geometries in heave by the LS-GCI method in Capytaine (CP) and WAMIT (WM).

| **Shape** | **Code** | **Uncertainty** | **0.66 [Hz]** | **1.147 [Hz]** | **1.635 [Hz]** | **2.163 [Hz]** | **2.65 [Hz]** |
|---|---|---|---|---|---|---|---|
|  WaveBot | CP | $U_{AM}$ [%] | 0.4 | 0.4 | 0.5 | 0.7 | 1.7 |
| | WM | $U_{AM}$ [%] | 0.1 | 0.0 | 0.1 | 0.3 | 471.4 |
| | CP | $U_{RD}$ [%] | 0.3 | 0.2 | 0.9 | 3.9 | 3.3 |
| | WM | $U_{RD}$ [%] | 0.2 | 0.2 | 0.4 | 0.7 | 470.7 |
|  Equal Draft Hat | CP | $U_{AM}$ [%] | 1.3 | 2.1 | 1.1 | 0.9 | 0.5 |
| | WM | $U_{AM}$ [%] | 1.0 | 1.1 | 1.0 | 0.8 | 0.8 |
| | CP | $U_{RD}$ [%] | 3.2 | 24.0 | 6.1 | 4.1 | 1.9 |
| | WM | $U_{RD}$ [%] | 1.4 | 10.6 | 3.4 | 2.1 | 1.5 |
|  Equal Volume Hat | CP | $U_{AM}$ [%] | 1.0 | 1.5 | 0.4 | 0.7 | 2.0 |
| | WM | $U_{AM}$ [%] | 4.1 | 5.6 | 7.4 | 6.9 | 5.8 |
| | CP | $U_{RD}$ [%] | 1.6 | 2.8 | 8.7 | 18.7 | 10.2 |
| | WM | $U_{RD}$ [%] | 1.4 | 13.1 | 74.9 | 151.8 | 67.8 |

Most of the mesh convergence rates were oscillatory at higher frequencies, and this results in uncertainties that are multiple factors of the value of added mass and/or radiation damping (e.g., WAMIT WaveBot values for 2.65 Hz frequency). This is likely due the application of high factors of safety by the LS-GCI tool in response to a perceived low quality estimation. The WAMIT simulations were consistently displaying iterative solver errors at higher frequencies, so it is likely that these results are inconsistent in only this code for this reason. For both GCI and LS-GCI results, we see consistently higher mesh uncertainty for radiation damping when compared to added mass. For added mass, the uncertainties do not vary significantly, so the average uncertainty of around $0.5\%$ for WaveBot, $1.1\%$ for the equal draft hat, and $3.5\%$ for the equal volume hat are subsequently used. This is excluding outliers, defined as values greater than $20\%$. The average uncertainty excluding outliers for radiation damping is approximately $1.2\%$ for WaveBot, $4\%$ for equal draft hat, and $8\%$ for equal volume hat. Even with no irregular frequency removal, Capytaine has low uncertainty

in most cases, even for frequencies where grid refinement in WAMIT suggests high errors.

Directly comparing the GCI and LS-CGI results in Tables 3.2 and 3.3, we see that LS-GCI results have consistently higher uncertainties. This could be due to the more conservative approach of LS-GCI, that accounts for quality of the estimation based on convergences, and scales the errors to higher uncertainties in response.

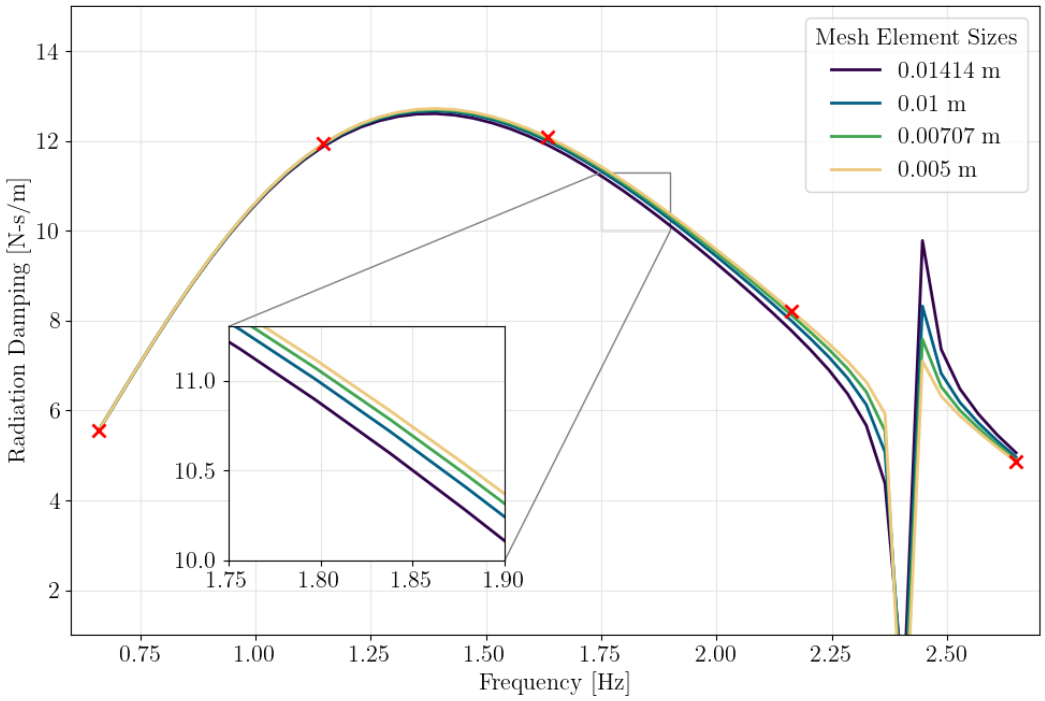


**Figure 3.2:** Evidence of mesh convergence for the WaveBot radiation damping coefficient in heave with Capytaine. Red 'x' markers indicate the five frequencies that GCI and LS-GCI analyses were conducted at.

To visualize the convergence across all frequencies in more of a qualitative sense, Figure 3.2 shows radiation damping in heave for WaveBot for each mesh tested in Capytaine. This involves the full range of frequencies, as opposed to the discrete frequencies used in the convergence study. Radiation damping converges tightly with mesh refinement at some frequencies, but not at all frequencies, particularly around the numerical artifact at $\sim 2.4$ Hz. Overall, the spread in the reported values with mesh refinement appear to be smaller than suggested than the formal uncertainty analysis from either the GCI or LS-GCI methods. For example, at 2.2 Hz, the spread in radiation damping between the two most refined meshes is considerably

less than 4% of the radiation damping.

The estimates of uncertainty presented above were referencing the second most refined mesh, of element size 0.00707 m with mesh statistics as shown in Table 3.1. These analyses were repeated for the most refined mesh of element size 0.005 m, with similar convergence trends in the GCI results, and similar non-physical uncertainty estimations at higher frequencies for the LS-GCI analysis. The final component to grid refinement studies is determining which level of mesh refinement balances the trade-off between computation time and uncertainty. More refined meshes require significantly more computation time, and so we must determine an acceptable level of uncertainty that still allows us to complete simulations in a reasonable time period. Figure 3.3 is a visualization of this trade-off for the LS-GCI results calculated with WAMIT.

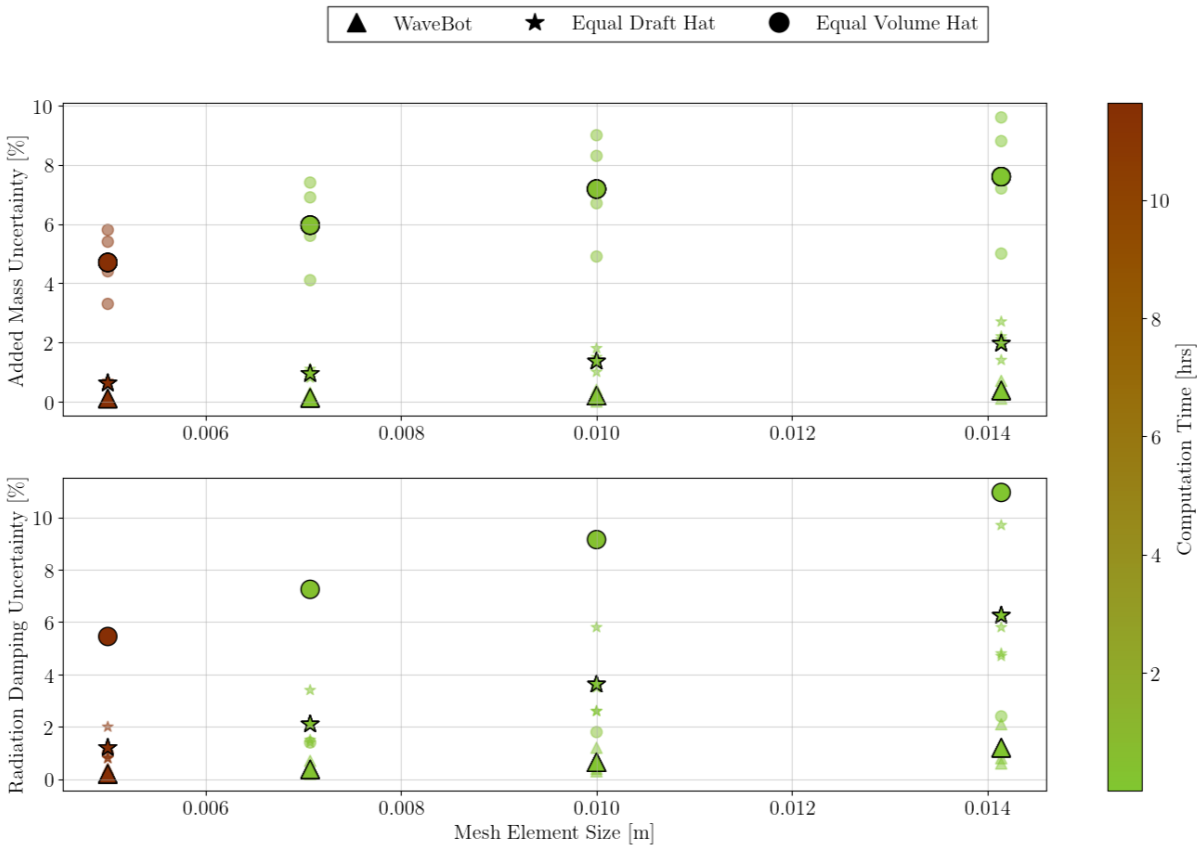


**Figure 3.3:** Added mass and radiation damping uncertainties for each mesh refinement level across three geometries with WAMIT. Markers are colored according to computation time. Outlined, larger markers indicate the average uncertainty for the given shape and parameter. Shaded, smaller markers indicate the uncertainty at each of the five frequencies.

In Figure 3.3 we see that every mesh refinement level other than the most refined has a computation time of less than one hour for all parameters and geometries. The uncertainty estimations between the most refined and next smallest meshes ($0.005$ m and $0.00707$ m, respectively) are not significantly different for WaveBot or the equal draft hat, which indicates that there are limited gains in solution precision at these levels of refinement. If we set our uncertainty threshold at $8\%$ for both added mass and radiation damping, the two most refined meshes would be acceptable for all three geometries, and the uncertainties for WaveBot and the equal draft hat are well below this $8\%$ maximum. Keeping in mind the limited decrease in uncertainty and the much higher computation time required for the smallest mesh, the second most refined mesh of element size $0.00707$ m is the mesh used in future results for all three BEM codes.

# Chapter 4

# BEM Validation for the Benchmark Case

With an estimation of discretization uncertainty and an optimal mesh balancing computational expense against accuracy from the solution verification analysis, the next step in validating BEM is confirmation of correct software operation. For this step, we use the WaveBot geometry. First, we compare the results of each of the three BEM models against one another, then we compare these results against existing BEM and experimental data for WaveBot.

## 4.1 Code Comparisons

For code comparison, we use WaveBot in each of our three BEM models to see if there are any strong variations between codes. We do not expect significant difference between results from different models, since all three codes utilize similar theories to guide their unique numerical implementation. To check this, the added mass, radiation damping, and excitation force for the WaveBot geometry in heave, surge, and pitch were compared for all three codes. As shown in Figure 4.1, there is limited variation in the codes for all parameters in heave and surge, but not in pitch. WAMIT seems to consistently underpredict the pitching coefficients for all parameters. This arises from WAMIT's calculation of moments about the still water line instead of the center of gravity, as in Aqwa and Capytaine. This could be corrected by applying a transformation matrix or by changing the body fixed coordinates in WAMIT.

When tabulated, the average relative error between WAMIT and Capytaine is less than 3.5% of the given hydrodynamic parameter for all non-rotational degrees of freedom. The relative error between WAMIT

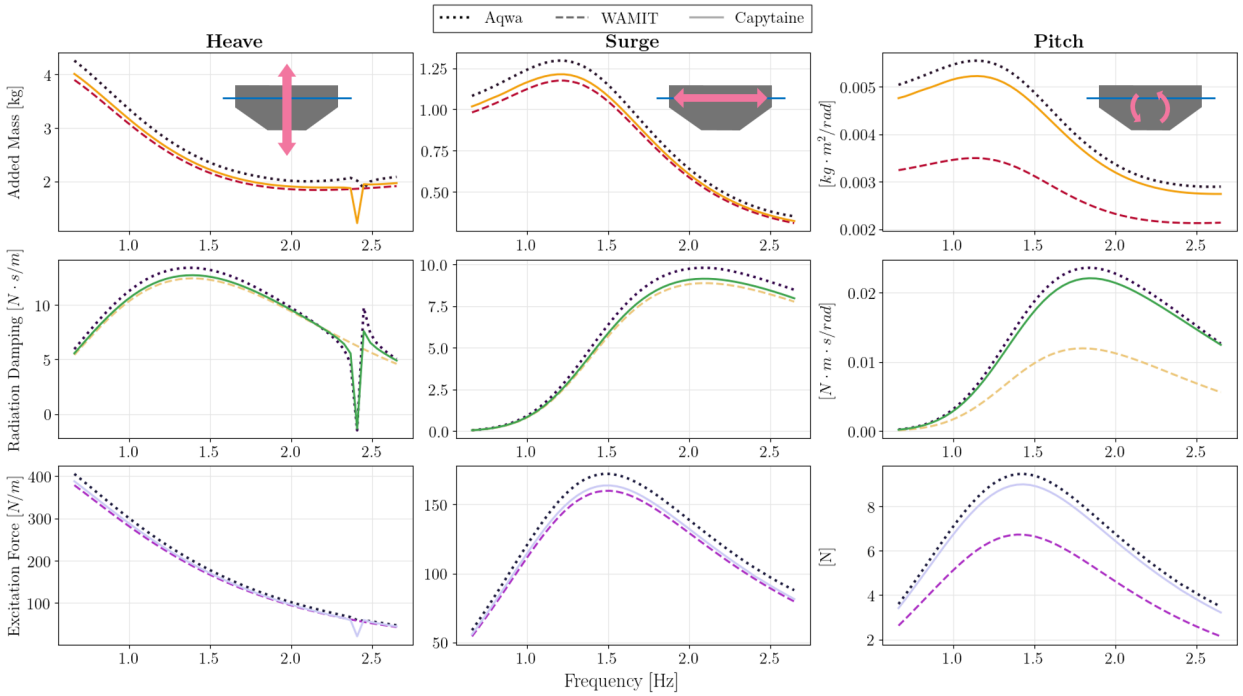


**Figure 4.1:** Comparison of BEM codes across surge, heave, and pitch degrees of freedom and added mass, radiation damping, and excitation force hydrodynamic parameters for the lab-scale WaveBot geometry

and Aqwa, which have the most visible differences in results, is less than 10% in all non-rotational cases. Every result presented in the following sections was replicated across all three BEM codes to fully ensure that the code variations were trivial. Variation between BEM codes was similarly low for the additional geometries considered. As a result, the experimental-BEM comparisons included in this thesis use WAMIT. The remainder of our analysis focuses on heave motion, so the discrepency in pitch for WAMIT will not be a problem.

## 4.2 Sandia Experimental Methods

The Sandia WaveBot is 1/17th model of a full-scale WEC with multiple degrees of freedom that can be locked and unlocked to allow for a number of configurations. The float geometry is designed to provide mostly linear dynamics in single degree-of-freedom experiments [23], which should result in strong agreement between experiments and BEM modeling. The float has added ballast weight to bring it to equal mass and displaced mass at the static position.

Testing occurred at the Manuevering and Seakeeping basin (MASK) at the Naval Surface Warface Center in Bethesda, Maryland. The MASK basin has a depth of 6.1 m, width of 73 m, and length of 110 m, and is spanned in length by a bridge with rotational capabilities [23]. There is a carriage mounted below the bridge that can translate along rails for mounting models and instrumentation, in this case, the WaveBot and test device structure. The tests described here were an initial suite known as MASK1. Most of the testing in [23] focused on movement in heave, with the ability to lock out motion for excitation tests and induce heave motion for forced oscillation tests. Subsequent tests do not allow added mass, radiation damping, and excitation to be directly extracted for single degrees of freedom.

Two types of tests were conducted: forced oscillation and wave excitation. In the forced oscillation tests, the water was completely still, and the buoy motion is forced by an actuator. The measured vertical position of the buoy and force on a load cell allow for the estimation of radiation damping and added mass coefficients. In the wave excitation or diffraction tests, the device was locked to be completely rigid and is subject to incoming waves from a chosen direction. The forces measured on the load cell on the device can be used to calculate the total excitation force from the incident and diffracting waves. Tests were conducted with inputs of monochromatic waves, idealized ocean states based on a Bretschnieder spectra, and four kinds of multisine signals for the forced oscillation, wave excitation, and dynamic response testing. For this analysis, we focus on monochromatic waves. The monochromatic tests were conducted with at combinations of frequencies and amplitudes: $f = [0.25, 0.30, 0.40, 0.50, 0.60, 0.65, 0.70, 0.80, 0.90, 1.00]$ Hz and wave amplitudes of 0.025, 0.05, and 0.1 m. For more information about this suite of tests, refer to [23]. Since these tests were conducted, there have been four more MASK testing campaigns that studied more complicated dynamics, with updated experimental, data collection, and processing methods.

## 4.3 Results

The BEM simulations for this comparison were performed for both the Sandia-scale and lab-scale versions of WaveBot. The experimental results for comparison were recreated from the relevant MASK1 test data [30] using the methods outlined in [23]. The re-created experimental results were then compared to simulations of WaveBot at the 3D-printed scale that were Froude-scaled to the Sandia 1/17th commercial scale. Figure 4.2 shows the Sandia experimental data for added mass and radiation damping, and the Sandia

WAMIT results compared to our scaled WAMIT simulations.

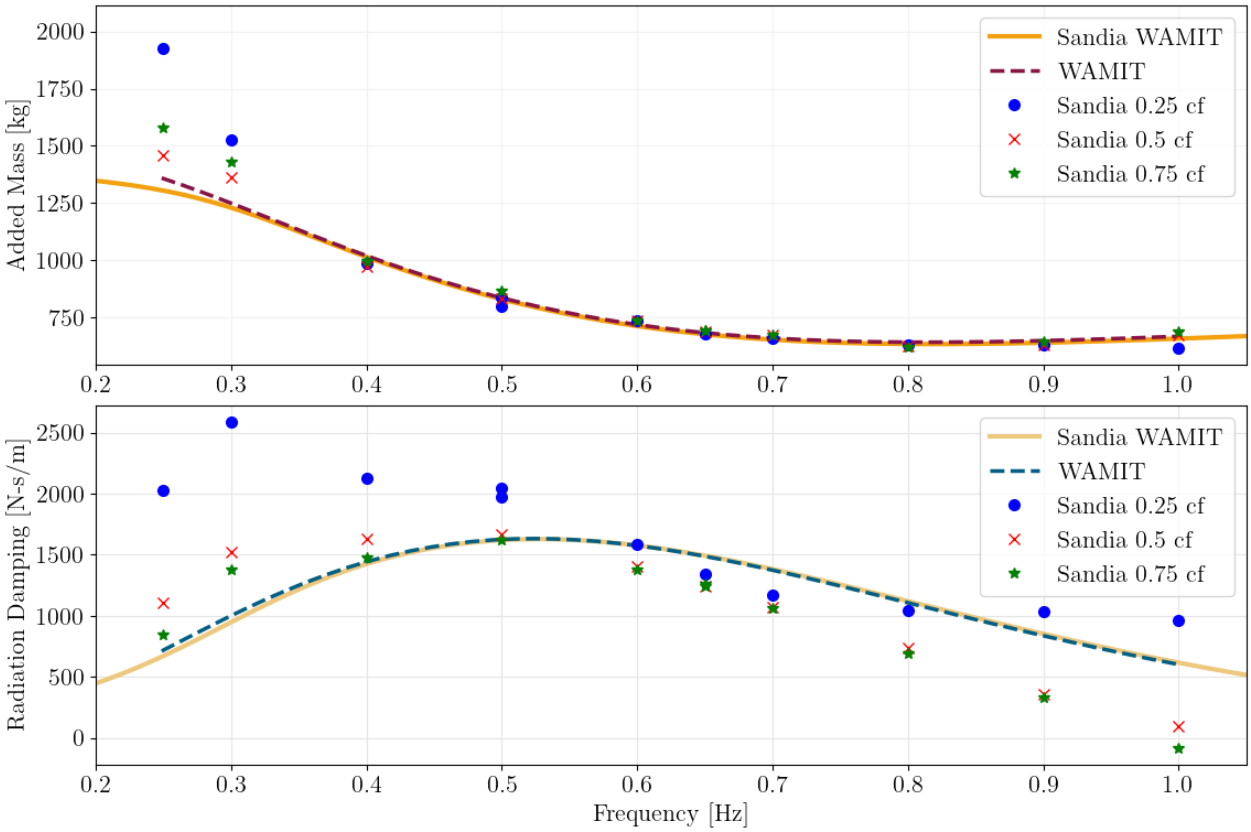


**Figure 4.2:** Comparison of Sandia WaveBot added mass and radiation damping experimental and BEM results with our WAMIT BEM results for heave motion. The amplitudes are represented as "cf" or current fraction of the actuator, but likely correspond to wave amplitudes of 0.025, 0.05, and 0.1 m listed in the report [23] since higher currents would be required to drive higher amplitude oscillations.

For added mass, the BEM results align closely with the experimental results for every amplitude, with the exception of lower frequencies, though signal to noise ratios are lowest for these data points. The same trend is seen in the Sandia WAMIT results when compared to experimental added mass values. For radiation damping, there is less agreement between BEM and experimental results, but BEM tracks the amplitude trend with frequency. This level of agreement is observed in the Sandia WAMIT results as well. For both added mass and radiation damping, the Sandia WAMIT code and our WAMIT code produce near identical results, which validates our operation of the WAMIT code. Since this result is repeatable across BEM codes, this validates our operation of Capytaine and Aqwa, as well.

# Chapter 5

# Experimental Validation

With a confirmed BEM procedure, and estimated uncertainty from both mesh refinement and code comparisons, we move to BEM comparison with experimental data for each geometry. Areas of agreement and disagreement based on geometry, frequency, amplitude, and hydrodynamic coefficient are explored to evaluate potential non-linear behavior that is not captured by BEM. Experiments and associated data analysis were primarily performed by Sarah Palmer, with my support.

## 5.1 Experimental Methods

The lab-scale experiments for the WaveBot and equal draft hat were performed in the Harris Hydraulics laboratory in Seattle, Washington, The forced oscillation experiments used the oscillation visualization tank, and the wave excitation experiments used the Washington Air-Sea Interaction Research Facility (WASIRF). The oscillation visualization tank is an acrylic cube with an open top with dimensions: 1.27 m long, 1.27 m wide, and 1.45 m high with a maximum water depth of 1.2 m [31]. WASIRF is an open-channel flume with a wavemaker, 12 m long, 0.91 m wide, and 1.22 m deep with a maximum water depth of 0.75 m. WASIRF has a shallow sloped absorption beach opposite from the wavemaker to decrease reflections, and can produce regular waves with amplitudes less than 10 cm and periods between 0.7 and 10 Hz [31].

The physical models were 3D printed using PETG, and then coated with epoxy to ensure the mass remained constant and no water was absorbed during the experiments, since this would change the mass and center of mass. The mass of WaveBot was 1.343 kg, and the equal draft hat was 1.272 kg. Neither of

these masses are equivalent to the displaced mass of water at the chosen still waterline position of 2.84 cm below the top of the buoy. These measured masses were used in BEM simulations, with the knowledge that any warnings due to prescribed mass – displaced mass not aligning could be ignored because this change will only impact the BEM calculation of hydrodynamic stiffness, but not added mass, radiation damping, or wave excitation.

In the forced oscillation experiments, forces and torques on the test article were measured with a 6-axis load cell (ATI mini40) and position measured with an encoder. The oscillations were driven by an actuator with a velocity control scheme, and both load cell tares and buoy position drift tests were taken periodically to correct for these sources of error. Oscillation tests were driven at amplitudes of 0.0115 m, 0.023 m, and 0.03 m at the Froude-scaled Sandia frequencies between 0.66 Hz and 2.65 Hz. The 0.03 m tests occurred at a lower waterline to ensure that the brim of the hat did not exit the water during oscillations, and so are not included in the results. The oscillation tank is relatively small compared to the size of the model, so we expect that reflections of the induced waves will have occurred during each test.

The wave excitation experiments used a 6-axis load cell to measure forces and torques due to incident waves, and wave gauges at various positions along the length of the tank to measure free-surface elevation. The buoy model was 1/3 of WASIRF's width, which is an upper limit for neglecting wall interaction. The wave frequencies were the same as for forced oscillation tests, but with amplitudes of 0.0058 m, 0.0115 m, and 0.023 m amplitude. The water depth was 0.648 m for all tests, which places the waves within either transitional or deep water conditions. The wave theory corresponding to the prescribed wave conditions varies from linear small amplitude Airy at lower amplitudes and frequencies, to Stoke's 5th order theories just below breaking at the highest amplitudes and frequencies. Visual record of the tests shows that non-Airy wave shapes and wave breaking often occurred at higher frequencies while testing, so we expect to see more non-linear behaviors for these cases, and likely a higher mismatch with BEM.

## 5.2 Results

The settings in the BEM simulations for this comparison followed the experimental conditions as closely as possible, with the exception of depth, which was found to have little impact on predicted hydrodynamic coefficients. The experimental data was analyzed by a series of different time and frequency-domain methods,

and the method with the best agreement over all conditions is shown in the following results. Added mass and radiation damping coefficients are calculated with a time-domain method, and excitation forces with a frequency-domain method. Figure 5.1 shows the experimental and BEM results for the WaveBot and equal draft hat geometries in heave.

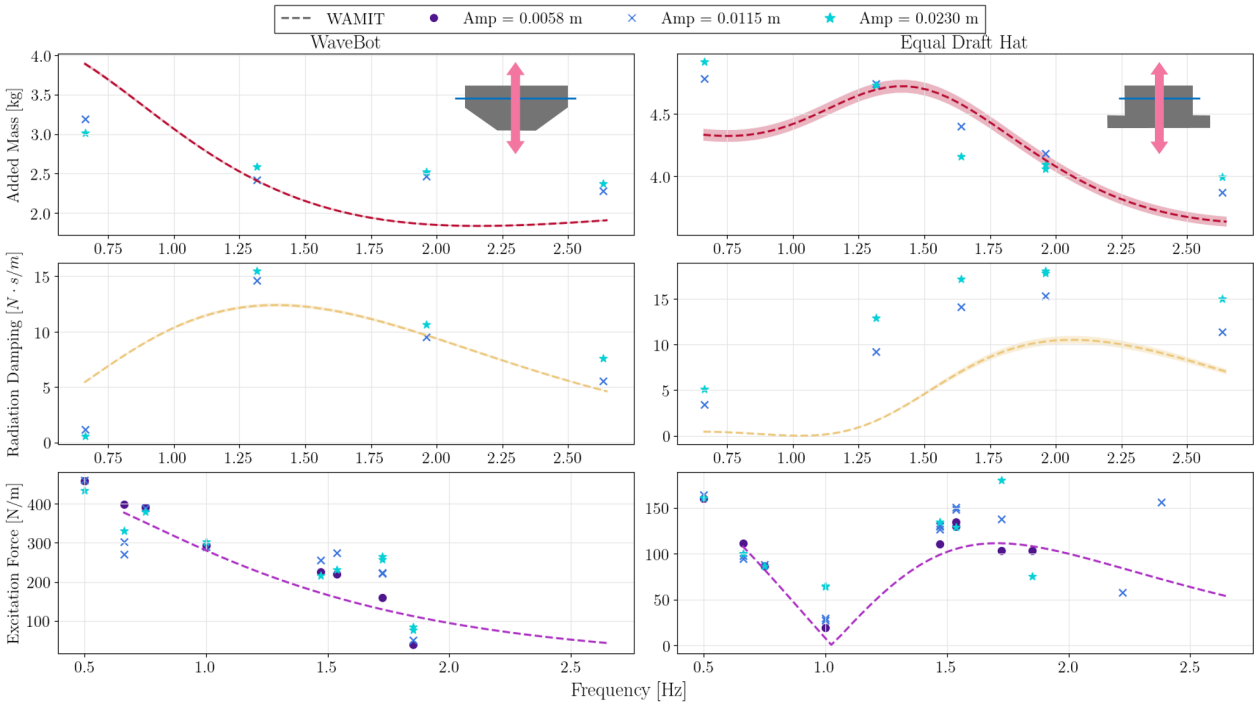


**Figure 5.1:** Experimental and BEM parameter comparison for WaveBot and equal draft hat geometries in heave. Shaded regions for added mass and radiation damping indicate uncertainty due to mesh refinement.

Beginning with WaveBot, there is good agreement across most frequencies for the radiation damping coefficient. The shape of the experimental curve matches closely with BEM, with slightly less close agreement on the magnitude of damping. Viscous damping effects are grouped with the radiation damping estimated from experiments, but are not present in BEM due to potential flow assumptions. This suggests that, for the WaveBot in our wave frequency range, the magnitude of viscous damping is likely low. Added mass has less agreement. Both experimental and BEM curves for WaveBot follow the trend of decaying to a constant value with increasing frequency, but BEM overpredicts at low frequency and underpredicts at higher frequencies. One potential reason for this disagreement at higher frequencies (which was not seen in the Sandia experiments), is reflections from the walls of the oscillation tank, resulting in more fluid motion near

the buoy, and more expected added mass.

For the hat geometry, there is better agreement for added mass over all frequencies except the lowest tested frequency. The experimental results fall within the expected uncertainty in the calculation due to geometric discretization at 1.3 Hz and 1.9 Hz frequencies. For radiation damping, the trend of both experimental and BEM curves is the same, but BEM consistently underpredicts the damping coefficient. This makes sense because the experimental damping includes viscous damping, which is likely appreciable for this sharp-edged geometry.

For excitation tests for both geometries, there is good agreement at low frequencies for all amplitudes. The behavior of the excitation force with frequency is effectively captured at low frequencies for all amplitudes, and at all frequencies for the lowest amplitude test. Starting at around 1.5 Hz, the experimental results begin to diverge for two higher amplitude tests (0.0115 m and 0.023 m). This is consistent with the observed transition in the incident waves from Airy to higher order theories, which cannot be captured by BEM.

Overall, for both geometries, there is better agreement for the lower wave amplitude tests. Because of the underlying linear assumptions, BEM estimates are independent of amplitude. In reality, lower amplitude waves have lower steepness and thus generally follow linear wave theory, and would exhibit similar amplitude independence. Higher amplitude waves, with potentially higher steepness could be more nonlinear depending on period and wavelength, and so there could be an amplitude dependence to the results, which is seen in the higher deviation from BEM. The amplitude dependence is more pronounced in the hat geometry than in WaveBot, suggesting the linear assumptions break down earlier for some geometries.

## 5.3 Discussion

Our results demonstrate that BEM can correctly predict the behavior of hydrodynamic coefficients with frequency for different geometries. For all compared cases, the trends of the curves match with frequency. BEM can more accurately estimate the magnitude of these coefficients in cases where viscous damping is negligible in comparison to radiation damping and for small amplitude wave conditions.

There is not enough information to confirm if the differences in BEM agreement between the two geometries can be attributed to geometric features like the brim of the hat or the conical portion of the WaveBot.

With more research into wave conditions, and a keener choice of frequencies and amplitudes, we may be able to decrease the presence of non-linear wave states and focus more on hydrodynamic effects due to geometric features. Additionally, further experiments that could quantify the viscous damping, or decrease the potential presence of reflections in the data. This could help attribute some of these errors more definitively to specific BEM assumptions like that of an inviscid fluid.

Though our results show some disagreement between BEM and experiments, this does not give us an estimation of how these differences might influence the energy capture capabilities of the WEC or how the difference in agreement between parameters will influence the overall WEC behavior. However, this is not a simple undertaking. Our initial thought was quantify this through a single, reduced parameter of hydrodynamic radiation force, which combines the behavior of radiation damping and added mass with corresponding velocity and acceleration of a prescribed sinusoid. However, because most of the radiation force is attributed to added mass, this does not accurately capture the importance of radiation damping on the power absorption for a WEC. A time-domain simulation such as one created by Aqwa 'Hydrodynamic Reponse' or WEC-Sim, may be able to provide more information about how the BEM errors or experimental artifacts propagate into overall WEC performance.

# Chapter 6

# Geometry and Hydrodynamics

BEM simulations were performed on two additional geometries beyond those of experiments to gain insight into how the hydrodynamic parameters vary with buoy geometry. The additional hat geometries were designed to reveal if maintaining submerged volume, wetted surface area, or draft would allow for better comparison of hydrodynamic parameters between distinct geometries.

## 6.1 Results

This geometric study was performed for three degrees of freedom with all three BEM codes. The hydrodynamic parameters in heave are shown in Figure 6.1 for each of the geometries described in Chapter 2.

As shown in Figure 6.1, both added mass and radiation damping are strongly geometry-dependent in heave, with geometry also driving different frequency dependence. For added mass, each of the hat geometries appear to decay to the same constant value with increasing frequency, which could indicate that the asymptotic added mass at higher frequencies is a function of overall geometry, and not of submerged volume, wetted surface area, or draft. The equal draft hat has a local maximum that is not present in any other geometry curve for added mass, but this may be a consequence of the lowest resolved frequencies. Additional investigation (not shown) demonstrates that the WaveBot does have a local maximum around 0.45 Hz.

With closer observation, it appears that the equal draft hat is more of an outlier geometry than the other two hat geometries compared to WaveBot. This is clearest in the radiation damping results. While the

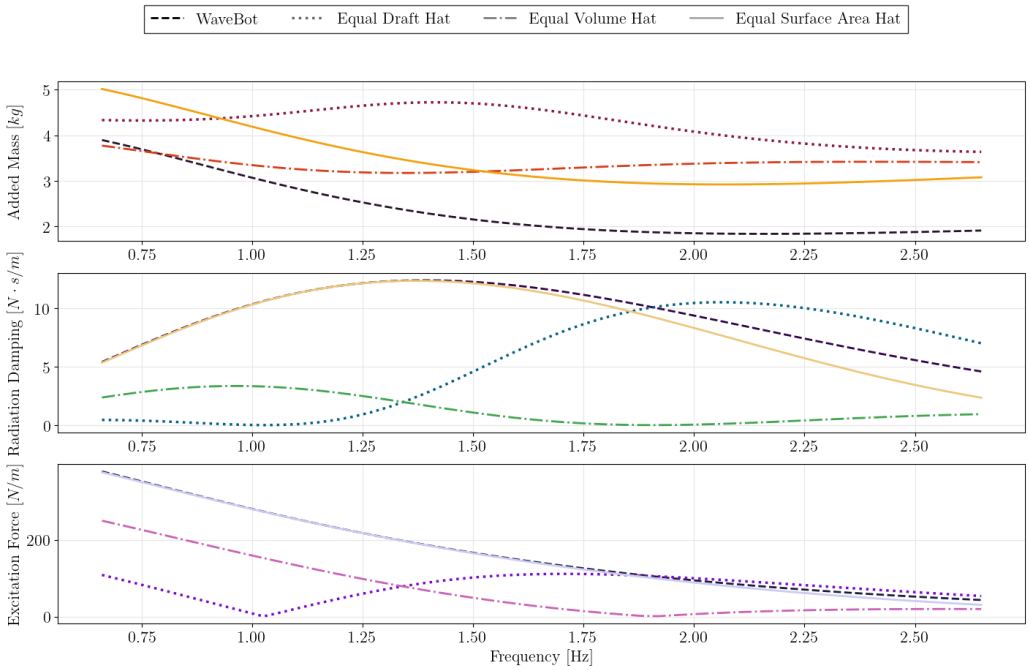


**Figure 6.1:** Comparing hydrodynamic parameters across geometries for heave motion.

magnitudes are all different, each of the other three geometries do follow similar trends with shifted peaks in radiation damping. If our frequency range was extended lower, the three geometries may exhibit the initial low magnitude of the equal draft hat.

For excitation results, the equal draft hat again presents different behavior than the other three geometries. The other three geometries decay consistently across the frequency range, with similar behavior between the WaveBot and equal surface area hat. Strong agreement in magnitude and behavior of radiation damping and excitation force is seen for frequencies less than 1.75 Hz for the WaveBot and equal surface area hat geometries. This could indicate some dependence of radiation damping and excitation force on wetted surface area. In fact, for all three parameters including added mass, the equal surface area hat follows nearly the same trend as WaveBot, with different magnitude for added mass.

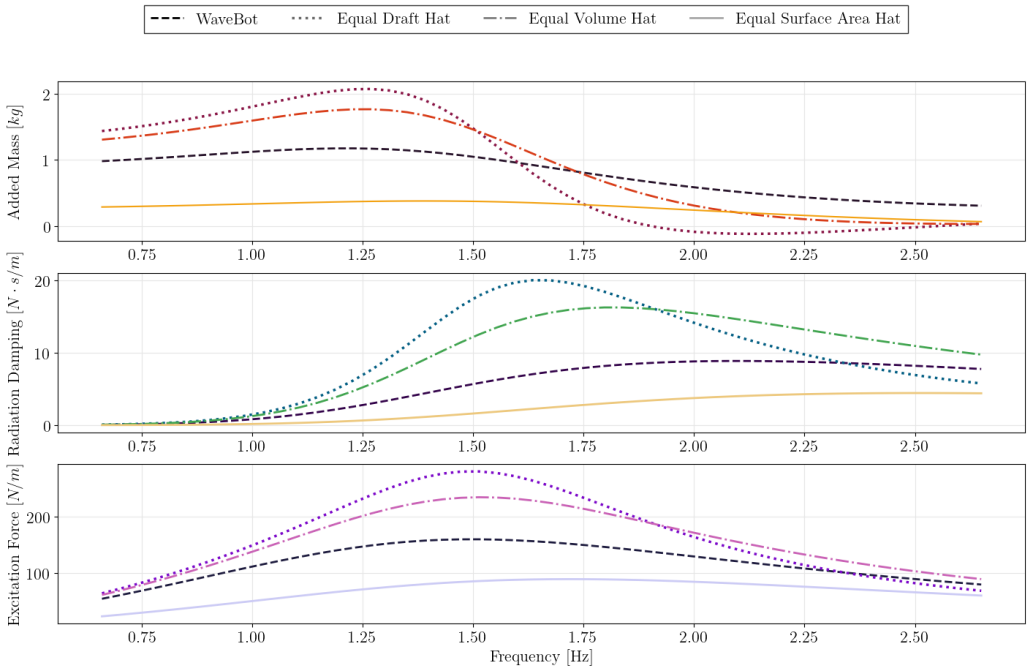


**Figure 6.2:** Comparing hydrodynamic parameters across geometries for surge motion

Comparable results for motion in surge are presented in Figure 6.2. There is less of a distinction between the equal draft hat and the other geometries in this degree of freedom, though most of the other observations for heave still hold true. The equal surface area hat and WaveBot still correspond most closely in behavior, but do not directly overlap in magnitude as seen in the heave results. One interesting feature is that the added mass briefly takes on a negative value for the equal draft hat. This has been observed in buoy shapes with moon pools, and submerged buoys near the free-surface [32], but is not found in the literature for a floating body with no interior free-surface. This could indicate that either BEM cannot accurately approximate added mass for this geometry, or that the submerged brim of the hat is approximating the behavior of a submerged buoy near the free-surface.

## 6.2 Discussion

Initially, it seemed the strong agreement between WaveBot and the equal surface area hat could indicate that BEM results are somewhat independent of geometry in trend, if not magnitude. However, if we revisit the actual shapes of the three hats, we see that only the equal draft hat has a large brim size. The equal surface

area hat has the smallest brim, and is therefore closest to a cylindrical-shaped buoy, and closer to WaveBot. In contrast, the equal draft hat has by far the largest brim, which likely contributes to its larger variation in hydrodynamic behavior with frequency.

There are two directions for further study in relation to this behavior. First, to see the impact of brim width on the hydrodynamics, we could start with a cylindrical buoy and slowly increase the diameter of the brim while keeping other dimensions constant. This would allow us to determine if the brim is causing most of the differences seen here. If instead we believe that the wetted surface area, submerged volume, or draft is more relevant to the results, then a third distinct shape (not WaveBot or hat-like) could be defined with variations with those parameters held constant with WaveBot. If similar trends are seen, we can develop a better understanding of which geometric parameters allow for better comparison within BEM results.

# Chapter 7

# Conclusions

This work aims to characterize the uncertainties in BEM codes and investigate sensitivities in BEM due to changing geometries of point-absorber WECs through solution verification procedures and validation with experimental data. Errors due to mesh refinement were investigated to find an estimate of uncertainty for a mesh balancing computational cost and accuracy. The relative error between BEM codes was then investigated for each parameter. The combination of these two uncertainties provides a baseline error associated with the BEM estimates. When simulation hydrodynamic parameters are then compared to experimentally determined parameters, any experimental results beyond the baseline error range of BEM can be identified as points where the assumptions in BEM theory may be causing inaccuracies due to the realistic flow state or experimental artifacts are present. These points are connected back to the geometries to try to identify which assumption may be influencing the observed difference. Results from this study could provide guidance whether BEM is suitable for obtaining accurate results for all geometries.

For solution verification in Chapter 3, we investigated two methods of calculating mesh uncertainty. We found that the LS-GCI method is more suitable for this application, and that mesh sensitivity was unequally distributed between BEM codes, and geometric shapes. This sensitivity was less than 10% in reasonable cases for a moderately refined mesh, despite varying levels and types of convergence for hydrodynamic parameters. Though the LS-GCI method was more flexible, it was still subject to numerical errors, and suggested unrealistically large uncertainties at high frequencies.

In Chapter 4, a comparison of hydrodynamic parameters across BEM codes revealed that open-source

solver Capytaine and well-established code WAMIT have agreement within 3% for all hydrodynamic parameters in non-rotational degrees of freedom. This is with the exception of at the location of irregular frequencies in Capytaine, but the code is being continuously improved, and so this may be resolved soon. ANSYS Aqwa had larger deviations in hydrodynamic parameters, closer to 10% relative error as a maximum at some frequencies. In regard to Capytaine and WAMIT, this indicates that the two codes can be used interchangeably with little impact to calculated parameters. This will help inform the choice of BEM code, and having the option of a free and open-source code with similar performance to commercial codes should remove a barrier to BEM simulation.

Chapter 4 also served as a "implementation check" for our BEM methods, through comparison of parameters for a geometry with published experimental results. We found that our calculation of hydrodynamic parameters using WAMIT closely matched the agreement between BEM and experiments seen in [23], thus confirming our BEM settings and methods.

In Chapter 5, the results from the lab-scale experiments are presented alongside the corresponding BEM results for motion in heave for two differing geometries. We found that for added mass and radiation damping, BEM could accurately estimate the behavior of the hydrodynamics across frequencies, and more accurately estimated the magnitude of the parameters for lower amplitude wave conditions. For excitation testing, BEM accurately estimated the magnitude and behavior of the excitation force for low amplitude waves. The behavior of the excitation force was also accurately captured for higher amplitude tests at lower frequencies. BEM consistently underpredicted the damping coefficient for the hat, likely due to viscous damping present only in experiments. Since BEM proved to accurately predict the behavior of parameters across frequencies, it should be suitable for evaluating whether a geometry is appropriate for local wave conditions. Results also indicated that BEM may be trusted to predict the magnitude of the hydrodynamic parameters in flow conditions with low wave amplitudes.

The hydrodynamics exhibited by various geometries were presented in Chapter 6 for surge and heave motions. This section highlights that the hydrodynamic parameters vary strongly with geometry, even when some geometric aspects are held constant. With more simulations, we may be able to determine which dimension of a hat shape most impacts the hydrodynamic response. We may also be able to determine whether wetted surface area or submerged volume matter for the magnitude or behavior of the parameters.

In addition to performing more BEM simulations, future work with additional experimental data for more geometries would be helpful in narrowing down which geometric features influence BEM accuracy. An upgrade of the experimental set-up to decrease potential reflections and noise in the data would help reassure that areas of disagreement with BEM are a factor of BEM assumptions and not experimental errors. Experimental results for additional geometries with a larger forced oscillation testing tank are in progress and will be available in a forthcoming paper. These results will include comparisons for surge and pitch, in addition to the current heave data.

Finally, this project focused mostly on the hydrodynamics surrounding heave motions in point absorber WECs but there are five more degrees of freedom to explore, and many more WEC archetypes. If further work on this subject for point absorbers proves to be instructive for WEC geometry optimization, it may be valuable to perform a similar series of comparisons on other WEC types. This thesis has just begun to lay a foundation for characterizing BEM accuracy with differing geometries, but with future work it should be able to provide guidelines for the use of BEM for WEC modelling.

# Bibliography


[1] Arthur Pecher and Jens Kofoed. *Handbook of Ocean Wave Energy*. Jan. 2017. ISBN: 978-3-319-39888-4. DOI: 10.1007/978-3-319-39889-1.

[2] Curtis J. Rusch. "Scaling of Point-Absorber Wave Energy Converter Hydrodynamics". PhD thesis. 2021, p. 104. URL: https://www.proquest.com/dissertations-theses/scaling-point-absorber-wave-energy-converter/docview/2594570191/se-2.

[3] Johannes Falnes. "A review of wave-energy extraction". In: *Marine Structures* 20.4 (2007), pp. 185–201. ISSN: 0951-8339. DOI: https://doi.org/10.1016/j.marstruc.2007.09.001.

[4] Brian J. Rosenberg, Tim R. Mundon, Ryan G. Coe, Eliot W Quon, Chris C. Chartrand, Yi-Hsiang Yu, and Jennifer A van Rij. "Development of WEC Design Loads: A Comparison of Numerical and Experimental Approaches: Preprint". In: (Oct. 2019). URL: https://www.osti.gov/biblio/1572263.

[5] Mahdiyeh Farajvand, Demián Garcıa-Violini, and John V Ringwood. "Characterising uncertainty and external disturbance sources in wave tank experiments for wave energy converter modelling". In: *Proceedings of the 15th European Wave and Tidal Energy Conference*. 2023.

[6] Emma C. Edwards and Dick K.-P. Yue. "Optimisation of the geometry of axisymmetric point-absorber wave energy converters". In: *Journal of Fluid Mechanics* 933 (2022), A1. DOI: 10.1017/jfm.2021.993.

[7] J M B P Cruz and S H Salter. "Numerical and experimental modelling of a modified version of the Edinburgh Duck wave energy device". In: *Proceedings of the Institution of Mechanical Engineers,*

*Part M: Journal of Engineering for the Maritime Environment* 220.3 (2006), pp. 129–147. DOI: 10.1243/14750902JEME53.

[8] Morten Bech Kramer et al. “Highly Accurate Experimental Heave Decay Tests with a Floating Sphere: A Public Benchmark Dataset for Model Validation of Fluid–Structure Interaction”. In: *Energies* 14.2 (2021). ISSN: 1996-1073. DOI: 10.3390/en14020269.

[9] Markel Penalba, Thomas Kelly, and John Ringwood. “Using NEMOH for Modelling Wave Energy Converters: A Comparative Study with WAMIT”. In: Aug. 2017.

[10] Vaibhav Raghavan, George Lavidas, Andrei Metrikine, Nikos Mantadakis, and Eva Loukogeorgaki. “A comparative study on BEM solvers for Wave Energy Converters”. In: Oct. 2022, pp. 441–447. ISBN: 9781003360773. DOI: 10.1201/9781003360773-50.

[11] Claes Eskilsson, Alex Abolfazl Shiri, and Eirini Katsidoniotaki. “Solution verification of WECs: comparison of methods to estimate numerical uncertainties in the OES wave energy modelling task”. In: *Proceedings of the European Wave and Tidal Energy Conference* 15 (Sept. 2023). DOI: 10.36688/ewtec-2023-426.

[12] A. Garcia-Teruel and D.I.M. Forehand. “A review of geometry optimisation of wave energy converters”. In: *Renewable and Sustainable Energy Reviews* 139 (2021), p. 110593. ISSN: 1364-0321. DOI: https://doi.org/10.1016/j.rser.2020.110593.

[13] Milad Shadman, Segen F. Estefen, Claudio A. Rodriguez, and Izabel C.M. Nogueira. “A geometrical optimization method applied to a heaving point absorber wave energy converter”. In: *Renewable Energy* 115 (2018), pp. 533–546. ISSN: 0960-1481. DOI: https://doi.org/10.1016/j.renene.2017.08.055.

[14] Siya Jin and Ron Patton. “Geometry Influence on Hydrodynamic Response of a Heaving Point Absorber Wave Energy Converter”. In: Aug. 2017.

[15] ANSYS Inc. *Aqwa Theory Manual*. 2022.

[16] Wamit Inc. *WAMIT v7.0 manual*. 2013.

[17] Matthieu Ancellin and Frédéric Dias. “Capytaine: a Python-based linear potential flow solver”. In: *Journal of Open Source Software* 4.36 (Apr. 2019), p. 1341. DOI: 10.21105/joss.01341. URL: https://doi.org/10.21105%2Fjoss.01341.

[18] Aurélien Babarit and Gérard Delhommeau. “Theoretical and numerical aspects of the open source BEM solver NEMOH”. In: *Proceedings of the 11th European Wave and Tidal Energy Conference (EWTEC2015)*. Nantes, France, 2015.

[19] Paul Schofield. *ANSYS Aqwa Review*. 2012.

[20] Thomas Kelly, Iñaki Zabala, Yerai Peña-Sanchez, Markel Penalba, John V. Ringwood, João C.C. Henriques, and Jesús M. Blanco. “A post-processing technique for removing ‘irregular frequencies’ and other issues in the results from BEM solvers”. In: 5 (June 2022), pp. 123–131. DOI: 10.36688/imej.5.123-131.

[21] Sandia National Labs. *WecOptTool*. 2020. URL: https://sandialabs.github.io/WecOptTool/index.html.

[22] Giorgio Bacelli, Ryan G. Coe, David Patterson, and David Wilson. “System Identification of a Heaving Point Absorber: Design of Experiment and Device Modeling”. In: *Energies* 10.4 (2017). ISSN: 1996-1073. DOI: 10.3390/en10040472.

[23] Ryan Geoffrey Coe, Giorgio Bacelli, David G. Wilson, and David Charles Patterson. “Advanced WEC Dynamics & Controls FY16 Testing Report”. In: (Oct. 2016). DOI: 10.2172/1330189.

[24] Wanan Sheng, Raymond Alcorn, and Tony Lewis. “Physical modelling of wave energy converters”. In: *Ocean Engineering* 84 (2014), pp. 29–36. ISSN: 0029-8018. DOI: https://doi.org/10.1016/j.oceaneng.2014.03.019. URL: https://www.sciencedirect.com/science/article/pii/S0029801814001085.

[25] P. J. Roache. “QUANTIFICATION OF UNCERTAINTY IN COMPUTATIONAL FLUID DYNAMICS”. In: *Annual Review of Fluid Mechanics* 29.Volume 29, 1997 (1997), pp. 123–160. ISSN: 1545-4479. DOI: https://doi.org/10.1146/annurev.fluid.29.1.123.

[26] Luís Eça, Guilherme Vaz, and M. Hoekstra. “A Verification and Validation Exercise for the Flow Over a Backward Facing Step”. In: Jan. 2010, pp. 14–17.

[27] L. Eça and M. Hoekstra. “A procedure for the estimation of the numerical uncertainty of CFD calculations based on grid refinement studies”. In: *Journal of Computational Physics* 262 (2014), pp. 104–130. ISSN: 0021-9991. DOI: https://doi.org/10.1016/j.jcp.2014.01.006.

[28] L. Eça, G. Vaz, S. L. Toxopeus, and M. Hoekstra. “Numerical Errors in Unsteady Flow Simulations”. In: *Journal of Verification, Validation and Uncertainty Quantification* 4.2 (July 2019), p. 021001. ISSN: 2377-2158. DOI: 10.1115/1.4043975.

[29] MARIN. *Verification Tools*. 2023. URL: https://www.marin.nl/en/research/free-resources/verification-and-validation/verification-tools.

[30] Ryan Coe. *Advanced WEC Dynamics and Controls, Test 1*. Feb. 2016. DOI: 10.15473/1460418. URL: https://mhkdr.openei.org/submissions/151.

[31] Pacific Marine Energy Center. *Harris Hydraulics Laboratory*. URL: https://www.pmec.us/testing/harris-hydraulics-lab.

[32] P. Mciver and D. V. Evans. “The occurrence of negative added mass in free-surface problems involving submerged oscillating bodies”. In: *Journal of Engineering Mathematics* 18 (1984), pp. 7–22. DOI: https://doi.org/10.1007/BF00042895.

[33] MARIN. *Numerical Uncertainty Analysis - User Manual*. Version 2023.12.0.

[34] Johannes Falnes. *Ocean Waves and Oscillating Systems*. Cambridge University Press, 2004. ISBN: 0-521-78211-2.

# Chapter A

# Appendix A: BEM Settings

The following appendix details the settings used in each of the BEM codes for this thesis.

## A.1 Aqwa Settings

**Table A.1:** Aqwa settings used in a standard simulation for this thesis.

| **Parameter** | **Value** | **Description** |
|---|---|---|
| Physics Preference | Hydrodynamics | Mesh type |
| Element size | 0.00707 m | Mesh element size |
| Method | Triangles | Only generate triangular elements |
| Water Depth | 6.1 m | Set water depth |
| Water Density | 1025 $kg/m^3$ | Set water density |
| Water size X | 100 m | Set field domain |
| Water size Y | 100 m | Set field domain |
| Point Mass | mass, center of gravity | Create a point mass at the center of gravity |
| Define Inertia Values By | Direct Input of Inertia | Input inertia rather than radius of gyration |
| Ignore Modeling Rule Violations | No | Don't ignore mesh quality check errors |
| Calculate Extreme Low/High | No | Don't calculate frequencies beyond the specified range |
| ASCII Hydrodynamic Database | Yes | Generate .LIS file |
| Generate AHD Pressure Output | Yes | Generate .AH1 file |
| Wave Directions | 1, 0 degrees | Specify number and direction of waves |
| Intervals Based Upon | Frequency | Use frequency inputs |
| Range | Manual Definition | Set frequency range manually |
| Lowest Frequency | 0.66 Hz | Set low frequency |
| Highest Frequency | 2.65 Hz | Set high frequency |
| Number of Int. Freq. | 48 | Choose number of frequencies between low and high |

## A.2 WAMIT settings

**Table A.2:** WAMIT settings used in a standard simulation for this thesis. See [16] for more information on each setting.

| Parameter | Value | Description |
|---|---|---|
| IOUTLOG | 1 | Include a copy of the log in results |
| IPERIN | 2 | Input frequency in rad/s |
| ISOR | 1 | Include source formulation |
| ISOLVE | 0 | Use iterative solver |
| ISCATT | 0 | Solve for total diffraction potential |
| IRR | 3 | Remove irregular frequencies |
| MONITR | 0 | Do not write FORCE output to the monitor |
| NUMHDR | 1 | Write headers to numeric output files |
| HBOT | -1 | Infinite depth |
| IRAD, IDIFF | 1,1 | Solve complete diffraction and radiation problems |
| NPER | -50 | Solve at 50 evenly spaced periods |
| PER(1), increment | 4.1469, 0.25517 | Highest period, and spacing |
| NBETA | 1 | Number of incident wave angles |
| NBODY | 1 | Number of bodies |
| XBODY | 0, 0, 0, 0 | Relationship between global coordinates and body fixed coordinates |
| IMODE | 1, 1, 1, 1, 1, 1 | Degrees of freedom to evaluate at |
| IOPTN (1-9) | 1, 1, 2, 1, 0, 0, 0, 0, 0 | Hydrodynamic parameters to be evaluated |
| NBETAH | 0 | Number of Haskind wave headings |
| NFIELD | 0 | Number of field points |

## A.3 Capytaine settings

**Table A.3:** Capytaine settings used in a standard simulation for this thesis. Empty brackets indicate a value that is specific to the geometry being evaluated.

| Command | Description |
|---|---|
| fb.add_translation_dof(name = "Heave") | Add heave and surge as degrees of freedom to evaluate for |
| fb.rotation_center = [] | Set rotation center to calculated center of gravity |
| fb.center_of_mass = [] | Override center of mass to calculated center of gravity |
| fb.mass = | Set mass |
| fb.add_rotation_dof(name = "Pitch") | Add pitch degree of freedom to evaluate for at center of rotation |
| np.linspace(0.66, 2.65, 50) | Create a vector of 50 frequencies to evaluate at |